An efficient second order ImEx scheme for the shallow water model in low Froude regime

Ralph Lteif, Maria Kazolea, Martin Parisot

An efficient second order ImEx scheme for the shallow water model in low Froude regime

Ralph Lteif

Lebanese American University, School of Arts and Sciences, Computer Sciences and Mathematics Department, Beirut, Lebanon

INRIA, Univ. Bordeaux, CNRS, Bordeaux INP, IMB, UMR 5251, 200 Avenue de la Vieille Tour, 33405 Talence cedex, France

Maria Kazolea

INRIA, Univ. Bordeaux, CNRS, Bordeaux INP, IMB, UMR 5251, 200 Avenue de la Vieille Tour, 33405 Talence cedex, France

Martin Parisot

INRIA, Univ. Bordeaux, CNRS, Bordeaux INP, IMB, UMR 5251, 200 Avenue de la Vieille Tour, 33405 Talence cedex, France

Abstract

This paper presents the development and analysis of a second order numerical method tailored for shallow water flows in regimes characterized by low Froude numbers. The focus is on modeling oceanic and coastal dynamics across different scales, with particular attention on the variation of the Froude number from 1 near the shoreline to significantly lower values offshore. Classical hyperbolic schemes, such as Riemann solvers, become inefficient in these deep water conditions. To address this challenge, a hybrid numerical approach is proposed where part of the system is treated implicitly, resulting in an ImEx (Implicit-Explicit) scheme that allows long time simulation using a CFL condition that is independent of the Froude number. To minimize the computational cost associated with solving linear systems, a fully segregated approach is used. In this method, the water height and hybrid mass fluxes are handled implicitly, while velocities are treated explicitly, thus avoiding large linear system resolutions. While various Runge-Kutta schemes are available for a second-order time integration, we chose here a Crank-Nicolson scheme to reduce the number of linear systems required. Spatial discretization is performed using a second-order MUSCL reconstruction. The novel scheme is demonstrated to be Asymptotic Preserving (AP), ensuring that a consistent discretization of the limit model, known as the "lake equations" is obtained as the Froude number approaches zero. Through a series of one- and two-dimensional test cases, the method is shown to achieve second-order accuracy for different Froude numbers. Additionally, the computational efficiency of the proposed method is compared with that of a fully explicit scheme, demonstrating significant time savings with the ImEx approach, particularly in scenarios governed by low Froude numbers.

Keywords: Shallow water equations, Implicit-explicit scheme, Low-Froude number, Crank-Nicolson, Finite-Volume.

Contents

1 Introduction **2**

2 Governing equations **3**

Email addresses: ralph.lteif@lau.edu.lb (Ralph Lteif), maria.kazolea@inria.fr (Maria Kazolea), martin.parisot@inria.fr (Martin Parisot)

2.1 Dimensionless formulation of the shallow water equations . . . 3
2.2 Limiting system . . . 5

3 Numerical scheme **6**
3.1 Implicit-Explicit (ImEx) Crank-Nicolson time discretization . . . 6
3.2 Fully-discrete numerical scheme . . . 7

4 Test cases **10**
4.1 1D Numerical tests . . . 11
4.1.1 Manufactured solution . . . 11
4.1.2 Moving steady-states . . . 11
4.1.3 Riemann problem . . . 13
4.1.4 Low Froude number gravity wave . . . 15
4.2 2D Numerical test . . . 15
4.2.1 2D cylindrical explosion problem . . . 15
4.2.2 2D potential solution with variable topography . . . 17
4.2.3 Traveling vortex . . . 18

5 Conclusion **20**

1. Introduction

The nonlinear shallow water equations (NSWE) aim to describe the behavior of shallow, incompressible, and inviscid fluid flows, playing a key role in simulating oceanic and atmospheric dynamics across various scales. These equations are widely used in the modeling of physical processes influencing environmental and geophysical events [13, 25]. Critical physical applications like atmospheric surges, tidal waves, tsunami propagation and inundation, involve complex multiscale phenomena where advection and acoustic-gravity waves interact. To describe the flow's time scale, the Froude number, Fr is employed. This dimensionless quantity represents the ratio of convective velocity to the speed of gravity waves.

At low Froude numbers, the NSWE describe flows characterized by slow movement of fluid particles and fast surface gravity waves propagation. In large-scale oceanic flows, Fr is typically around 10^{-2} [41, 2]. For example, in oceanic currents with a velocity of $U_0 \approx 1\ \mathrm{ms}^{-1}$ and a depth of $H_0 \approx 100$ m, Fr is approximately 0.03. It is important to emphasize that solving the shallow water equations in the zero Froude number limit poses significant difficulties for two main reasons. First, as the Froude number Fr decreases, the system transitions towards a singular limit, shifting from a hyperbolic to a mixed hyperbolic-elliptic form, which complicates the solution process due to non-uniform behavior as $\mathrm{Fr} \to 0$. This convergence problem is a well-known mathematical challenge, as explored in previous studies [17, 38, 39]. Second, low Froude number flows introduce stiffness in the system, making numerical approximations more difficult. To address these multiscale challenges, numerical methods must incorporate the Asymptotic Preserving (AP) property, enabling them to capture the correct behavior of the governing equations in the asymptotic limit as $\mathrm{Fr} \to 0$. Several AP schemes have been developed for the shallow water equations; see, for instance [36, 37, 5, 16, 24, 58]. Additionally, several specific models and AP numerical schemes have been proposed for the congested shallow water equations taking into account the roof constraint; refer to [27, 28, 49].

In contrast, a non-AP scheme may perform poorly, potentially leading to issues such as incorrect pressure scaling in the approximation [34] leading to large numerical dissipation becoming predominant before the physical phenomena [33] or the appearance of artificial oscillations. These oscillations, as analyzed by Dellacherie in [18], can arise from the loss of consistency for near-incompressible flow.

Conventional explicit solvers, like the Godunov method, struggle to accurately model low Froude number flows due to the CFL condition required for stability. The stiffness of the equations enforces an extremely small time step, leading to high computational costs [33, 34]. Consequently, the simulations are substantially slowed, and the large number of iterations results in excessive numerical diffusion, regardless of the scheme's order. This is expected to suppress the water surface elevation. In contrast, fully implicit time-stepping schemes allow for larger time steps while retaining the accuracy of the

numerical solution. However, the main disadvantage of such methods lies in the requirement to solve a system that can become highly nonlinear, primarily due to the convective fluxes present in the governing equations.

Over the past few decades, numerous efforts have been made in the literature to address these challenges, with considerable focus placed on semi-implicit discretization techniques [15, 32, 50, 57, 9]. In this framework, advection is treated explicitly while pressure is handled implicitly, leading to a stability condition governed solely by the main flow velocity, which approaches zero in the low Froude number regime. As a result, semi-implicit schemes are far more efficient than explicit methods under these conditions. They also benefit from reduced numerical viscosity and enhanced accuracy, as the implicit terms do not require additional stabilization. The concept of distinguishing between slow and fast time scales has been successfully interpreted as a flux splitting method, as noted in [55]. Building on this idea, significant research has focused on developing numerical methods that handle multiple time scales [23, 10, 14, 45], commonly referred to as all Mach solvers. A different strategy for handling multiple time scales involves implicit-explicit (ImEx) schemes. Developing such a scheme involves tackling several challenges. The primary task is to define the fluxes, which is typically managed using splitting techniques that differentiate the fast components from the slower ones. The traditional method for performing this splitting is to handle the acoustic subsystem implicitly, while maintaining an explicit approach for the transport terms; refer to [1, 6, 8, 48, 35, 20, 5]. A recent and seemingly more adaptable method is the reference solution (RS) approach. In this technique, the splitting is carried out with respect to a reference state, which is the solution of a suitably defined sub-system that can be evolved alongside the main equations. The RS method has been applied to shallow water flows in [58].

The efficient high order time integration is more challenging in the context of ImEx schemes. For time integration up to second order, a variety of options are available, many of which rely on different multi-stage or multi-step ImEx formulations [10, 20]. Nevertheless, these methods usually involve solving a significant number of linear systems. The novelty of this work lies in minimizing the number of linear systems that need to be solved. More precisely, we extend the first-order Implicit-Explicit Centered Potential Regularization (ImEx CPR) scheme introduced in [50] to achieve a second order accuracy in time by using the Crank-Nicolson scheme.

The outline of the paper is as follows. The governing equations in dimensional and non-dimensional form are presented in section 2. Section 3 presents the numerical scheme and its asymptotic preserving and well-balanced properties. Section 4 provides numerical verification in one and two horizontal dimensions, and the concluding remarks are drawn in Section 5.

2. Governing equations

2.1. Dimensionless formulation of the shallow water equations

In this paper, we focus on developing a numerical scheme designed for NSWE in the low Froude number regime. These equations describe fluid motion over a fixed bottom topography, with a free-moving surface at the top. They capture the conservation of water height and the balance of the momentum flux, often referred to as discharge. Let us consider a two-dimensional bounded domain $\Omega \in \mathbb{R}^2$, which is defined by the space coordinates $\mathbf{x} = (x, y)$, and a time interval with the time coordinate $t \in \mathbb{R}^+$. The governing system of equations is expressed as:

$$\begin{cases} \partial_t h + \nabla \,.\, (hU) = 0, \\ \partial_t (hU) + \nabla \,.\, (hU \otimes U) + g\nabla\Big(\dfrac{h^2}{2}\Big) = -gh\nabla z. \end{cases} \tag{2.1}$$

with $h(t, \mathbf{x})$ representing the water height and $h(t, \mathbf{x})U(t, \mathbf{x})$ describing the momentum, where $U(t, \mathbf{x}) = (u, v)^\top \in \mathbb{R}^2$ is the vertically averaged velocity field. The free surface is represented by $\zeta(t, \mathbf{x}) := h + z$, where $z(\mathbf{x})$ is the bottom topography, and g is the gravitational constant. These quantities are illustrated in Figure 1. System (2.1) constitutes a set of hyperbolic balance laws, which can be derived by vertically integrating the Navier-Stokes equations [26]. For given characteristic scales T_0, H_0, L_0, $U_0 = \dfrac{L_0}{T_0}$ we apply the standard non-dimensionalisation procedure by rewriting the NSWE (2.1) in the dimensionless variables

$$\widetilde{T} = \frac{T}{T_0}, \quad \widetilde{h} = \frac{h}{H_0}, \quad \widetilde{\mathbf{x}} = \frac{\mathbf{x}}{L_0}, \quad \widetilde{U} = \frac{U}{U_0}, \quad \widetilde{z} = \frac{z}{H_0}. \tag{2.2}$$

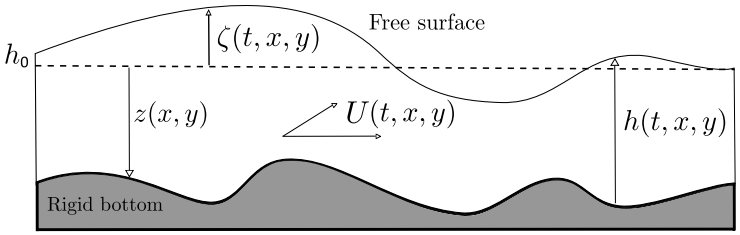

Figure 1: Key quantities in the two-dimensional case include the reference water height h_0, which is typically chosen to match the water level at rest.

This yields the following dimensionless form of the NSWE (2.1):

$$\begin{cases} \partial_t h + \nabla \,.\, (hU) = 0, \\ \partial_t (hU) + \nabla \,.\, (hU \otimes U) + \dfrac{1}{\mathrm{Fr}^2} \nabla\Big(\dfrac{h^2}{2}\Big) = -\dfrac{h}{\mathrm{Fr}^2} \nabla z, \end{cases} \tag{2.3}$$

where we have omitted the tildes for simplicity. Here, Fr represents the Froude number, defined as $\mathrm{Fr} = \dfrac{U_0}{\sqrt{gH_0}}$, which measures the ratio of the flow velocity to the speed of gravity waves.

In the vector form, the system (2.3) reads as

$$\partial_t V \;+\; \nabla \,.\, F(V) = S(V, z), \tag{2.4}$$

with $V = (h, hU)^\top$. The flux and source term are defined respectively as

$$F(V) = \begin{pmatrix} hU^\top \\ hU \otimes U + h^2 \mathbf{I}_2/(2\mathrm{Fr}^2) \end{pmatrix}, \quad S(V, z) = \begin{pmatrix} 0 \\ -h\nabla z/\mathrm{Fr}^2 \end{pmatrix}. \tag{2.5}$$

The eigenvalues of the system (2.4)-(2.5) in the normal direction $\mathbf{n} = (n_x, n_y)$ are given by

$$\lambda_1 = U \,.\, \mathbf{n} - \sqrt{h}/\mathrm{Fr}, \quad \lambda_2 = U \,.\, \mathbf{n} + \sqrt{h}/\mathrm{Fr}, \quad \lambda_3 = U \,.\, \mathbf{n}. \tag{2.6}$$

When discretizing the spatial domain Ω with Cartesian grid cells of size $\Delta x \Delta y$ and using an explicit method to solve the system (2.4)-(2.5), the CFL condition enforces the following time-step restriction:

$$\Delta t_{\mathrm{expl}} \leq \mathrm{CFL} \cdot \min\left(\frac{\Delta x}{\max\limits_{u,h} \left\{ |u| + \frac{1}{\mathrm{Fr}}\sqrt{h} \right\}}, \frac{\Delta y}{\max\limits_{v,h} \left\{ |v| + \frac{1}{\mathrm{Fr}}\sqrt{h} \right\}} \right) = \mathcal{O}(\mathrm{Fr}\Delta_{\min}),$$

where $\Delta_{\min} := \min(\Delta x, \Delta y)$ and $0 < \mathrm{CFL} \leq 1$. Furthermore, the numerical diffusion in explicit schemes is typically proportional to $\mathrm{Fr}^{-1}\Delta_{\max}^p$, where $\Delta_{\max} := \max(\Delta x, \Delta y)$ and p denotes the scheme's formal order. To prevent excessive numerical diffusion, one must select $\Delta x = \mathcal{O}(\mathrm{Fr}^{1/p})$ and $\Delta y = \mathcal{O}(\mathrm{Fr}^{1/p})$. As a result, the stability restriction for the time-step becomes $\Delta t = \mathcal{O}(\mathrm{Fr}^{1+1/p})$, which accounts for the significant computational cost associated with explicit methods in low Froude number regime. To circumvent the severe time step restrictions of explicit schemes, we consider using Implicit-Explicit time discretization, where slow waves are generally treated explicitly, while fast waves are handled implicitly.

The system defined in (2.3) admits non-trivial steady-state solutions governed by the following equations:

$$\begin{cases} \nabla \cdot (hU) = 0, \\ \nabla \cdot \Big(hU \otimes U + \dfrac{1}{2\mathrm{Fr}^2} h^2 \mathbf{I}_2 \Big) = -\dfrac{1}{\mathrm{Fr}^2} h \nabla z. \end{cases} \tag{2.7}$$

From these equilibrium conditions, various classes of steady-state solutions can be derived, as discussed in works such as [47, 52], which assist in evaluating the performance of numerical schemes. An important example of these solutions is the "lake at rest" state, obtained by assuming

$$U = 0 \quad \text{and a constant water surface elevation,} \quad \zeta = \zeta_0. \tag{2.8}$$

Recently, much research has focused on steady-state solutions in shallow water models. Significant efforts have been made to design numerical schemes that accurately preserve steady-states or at least a subset of them. These schemes are often referred to as *well-balanced* methods, or as preserving the *C-property* [4, 3, 42, 51]. To achieve the well-balanced property, which ensures that all non-temporal derivatives cancel out precisely at the discrete level in "lake at rest" steady-states, and to avoid the complexities of handling stiff source terms, the system (2.3) is reformulated by incorporating part of the flux terms into the bed-slope source term:

$$\begin{cases} \partial_t h + \nabla \cdot (hU) = 0, \\ \partial_t (hU) + \nabla \cdot (hU \otimes U) = -\dfrac{h}{\mathrm{Fr}^2} \nabla \zeta. \end{cases} \tag{2.9}$$

As a result, the new source term expressed in terms of the free surface variable $\zeta = h + z$ can be discretized using a straightforward second-order central difference method, preserving the well-balanced property.

The rest of this section is focused on discussing the asymptotic behavior of the dimensionless system (2.9).

2.2. Limiting system

To investigate the solutions of (2.9) as Fr approaches 0, a common approach [35, 5] is to consider the following single-scale expansions of the solutions h and U of (2.9), in terms of Fr:

$$\begin{cases} h(\mathbf{x}, t) = h_0(\mathbf{x}, t) + \mathrm{Fr}\ h_1(\mathbf{x}, t) + \mathrm{Fr}^2\ h_2(\mathbf{x}, t) + \cdots \\ U(\mathbf{x}, t) = U_0(\mathbf{x}, t) + \mathrm{Fr}\ U_1(\mathbf{x}, t) + \mathrm{Fr}^2\ U_2(\mathbf{x}, t) + \cdots \end{cases} \tag{2.10}$$

Since $\zeta = h + z$ with $z = z(x)$ being time independent, we have

$$\zeta(\mathbf{x}, t) = h_0(\mathbf{x}, t) + z(\mathbf{x}) + \mathrm{Fr}\ h_1(\mathbf{x}, t) + \mathrm{Fr}^2\ h_2(\mathbf{x}, t) + \cdots \tag{2.11}$$

Substituting (2.10) and (2.11) into (2.9), we isolate terms with same Froude powers. Extracting terms in Fr^{-2} yields:

$$-\frac{1}{\mathrm{Fr}^2} h_0 \nabla (h_0 + z) = 0 \Rightarrow h_0 \nabla (h_0 + z) = 0. \tag{2.12}$$

From (2.12) we immediately get that $h_0 + z \equiv H_0(t)$, namely, $h_0 + z$ is constant in space. This implies that, at leading order, the free surface must stay flat in wet areas. Moving forward, we gather the terms proportional to Fr^{-1} from the momentum equation in (2.9), leading to:

$$-\frac{h_0}{\mathrm{Fr}} \nabla h_1 - \frac{h_1}{\mathrm{Fr}} \nabla (h_0 + z) = 0 \Rightarrow h_0 \nabla h_1 = 0. \tag{2.13}$$

Assuming no dry area in the domain, namely $h(\mathbf{x}, \mathbf{t}) > \mathbf{0}$, the equation (2.13) allows us to conclude that $h_1 \equiv H_1(t)$ is also constant in space. Lastly, the terms of order Fr^0 extracted from (2.9) yield the following relations:

$$\begin{cases} (h_0)_t + \nabla . \ (h_0 U_0) = 0, \\ (h_0 U_0)_t + \nabla . \ (h_0 U_0 \otimes U_0) + h_2 \nabla (h_0 + z) + h_1 \nabla h_1 + h_0 \nabla h_2 = 0. \end{cases} \tag{2.14}$$

Since the bottom topography z is assumed to be time independent, (2.14) becomes

$$\begin{cases} \nabla . \ (h_0 U_0) = -\dfrac{dH_0(t)}{dt}, \\ (h_0 U_0)_t + \nabla . \ (h_0 U_0 \otimes U_0) + h_0 \nabla h_2 = 0. \end{cases} \tag{2.15}$$

Now integrating the 1st equation of (2.15) over the spatial domain Ω, it yields

$$\frac{dH_0(t)}{dt} = -\frac{1}{|\Omega|} \int_{\partial\Omega} h_0 U_0 . \ \mathbf{n} \ d\sigma, \tag{2.16}$$

where $\mathbf{n}$ is the unit outward normal vector along $\partial\Omega$. For some boundary conditions, e.g. periodic, wall, open boundary conditions, or under the sublinear growth conditions ($U_0(x)$, $h_0(x) = \mathrm{o}(|x|)$, $x \to \infty$) cf. [12], the integral cancels. As a consequence, the first equation of (2.15) gives:

$$\frac{dH_0(t)}{dt} = 0 \Rightarrow \nabla.\ (h_0 U_0) = 0.$$

(2.15) and (2.16) form the classical zero Froude number shallow water equations, also known as the "lake equations" which further reduce to:

$$\begin{cases} \nabla.\ (h_0 U_0) = 0,\ h_0 + z = H_0 = cst. \\ (h_0 U_0)_t + \nabla.\ (h_0 U_0 \otimes U_0) + h_0 \nabla h_2 = 0. \end{cases} \tag{2.17}$$

A rigorous convergence analysis for the zero Froude limit from (2.9) to (2.17) is very demanding (well prepared data), see [39] in the low Mach limit.

In the next section, we develop an asymptotic preserving scheme for (2.9), which yields a consistent approximation of the limiting equations (2.17) as $\mathrm{Fr} \to 0$.

3. Numerical scheme

3.1. Implicit-Explicit (ImEx) Crank-Nicolson time discretization

In this section, we develop a second order numerical scheme for the shallow water equations (2.9). In order to relax the strong stability restriction on the time-step size, we consider an implicit-explicit (ImEx) approach where the water height and hybrid mass fluxes are handled implicitly, while velocities are treated explicitly. High-order time integration poses significant challenges when working with ImEx schemes. For methods up to second order, several works exist in the literature, often employing various multi-stage or multi-step ImEx strategies, see [10, 20]. However, these approaches typically require solving a substantial number of linear systems. To address this issue, we opted for a Crank-Nicolson (CN) scheme, which minimizes the number of linear systems to be solved. To this end, we propose the following semi-discrete CN formulation of the NSWE (2.9):

$$h^{n+1} = h^n - \Delta t \nabla\ .\ \mathcal{F}^{n+\frac{1}{2}}. \tag{3.1}$$

where the upper indices n and $n+1$ corresponds to the current time level, t^n, and the new one, $t^{n+1} = t^n + \Delta t$ where Δt is the time step at the nth iteration, respectively. The numerical mass flux $\mathcal{F}^{n+\frac{1}{2}}$ is an approximation of $(hU)^{n+\frac{1}{2}}$ up to second order. More precisely, we set

$$\mathcal{F}^{n+\frac{1}{2}} = (hU)^n - \frac{\Delta t}{2} \nabla\ .\ \big((\widehat{hU})^{n+\frac{1}{2}} \otimes \widehat{U}^{n+\frac{1}{2}}\big) - \frac{\Delta t}{2\mathrm{Fr}^2} h^{n+\frac{1}{2}} \nabla \zeta^{n+\frac{1}{2}}, \tag{3.2}$$

where the following extrapolation reconstruction is used

$$\widehat{\psi}^{n+\frac{1}{2}} = \frac{3}{2}\psi^n - \frac{1}{2}\psi^{n-1}.$$

The main ingredient of the numerical mass flux is the presence of a regularizing term proportional to the gradient of the free surface [44, 54, 32, 50] which plays a similar role to the numerical viscosity introduced in the Lax–Wendroff scheme [40]. The upper index $n+\frac{1}{2}$ corresponds to the intermediate time level $t^{n+\frac{1}{2}}$ such that

$$\psi^{n+\frac{1}{2}} := \frac{\psi^n + \psi^{n+1}}{2}.$$

The nonlinear convective flux term in (3.2) is treated explicitly through extrapolation (Adams–Bashforth 2) which enables the separate resolution of the equations and avoid costly fully implicit time integration relying on the resolution of a large nonlinear system.

Once the nonlinear system (3.1) is solved, the new water depth h^{n+1} is known and the flow discharge is computed as follows:

$$(hU)^{n+1} = (hU)^n - \Delta t \nabla\ .\ \big((\widehat{hU})^{n+\frac{1}{2}} \otimes \widehat{U}^{n+\frac{1}{2}}\big) - \frac{\Delta t}{\mathrm{Fr}^2} h^{n+\frac{1}{2}} \nabla \zeta^{n+\frac{1}{2}}, \tag{3.3}$$

where the advection velocity and the advected discharge of the momentum equation are extrapolated.

In what follows, we show that the proposed semi-discrete scheme (3.1)-(3.3) in the low Froude number limit provide a consistent approximation of the limiting equations (2.17).

Theorem 1. *The semi-discrete scheme* (3.1)-(3.3) *is a consistent approximation of the low Froude shallow water system* (2.17) *at the leading order asymptotic expansion in the asymptotic limit (Fr* $\to 0$*).*

Proof. We consider first the following asymptotic expansions for the unknowns:

$$\begin{array}{l} h^n(\mathbf{x}) = h_0^n(\mathbf{x}) + \mathrm{Fr}\ h_1^n(\mathbf{x}) + \mathrm{Fr}^2\ h_2^n(\mathbf{x}) + \cdots \\ U^n(\mathbf{x}) = U_0^n(\mathbf{x}) + \mathrm{Fr}\ U_1^n(\mathbf{x}) + \mathrm{Fr}^2\ U_2^n(\mathbf{x}) + \cdots \\ \zeta^n(\mathbf{x}) = h_0^n(\mathbf{x}) + z(\mathbf{x}) + \mathrm{Fr}\ h_1^n(\mathbf{x}) + \mathrm{Fr}^2\ h_2^n(\mathbf{x}) + \cdots \\ h^{n-1}(\mathbf{x}) = h_0^{n-1}(\mathbf{x}) + \mathrm{Fr}\ h_1^{n-1}(\mathbf{x}) + \mathrm{Fr}^2\ h_2^{n-1}(\mathbf{x}) + \cdots \\ U^{n-1}(\mathbf{x}) = U_0^{n-1}(\mathbf{x}) + \mathrm{Fr}\ U_1^{n-1}(\mathbf{x}) + \mathrm{Fr}^2\ U_2^{n-1}(\mathbf{x}) + \cdots \\ \zeta^{n-1}(\mathbf{x}) = h_0^{n-1}(\mathbf{x}) + z(\mathbf{x}) + \mathrm{Fr}\ h_1^{n-1}(\mathbf{x}) + \mathrm{Fr}^2\ h_2^{n-1}(\mathbf{x}) + \cdots \end{array} \tag{3.4}$$

which are well-prepared initial data satisfying the low Froude number limits in (2.17) at time level t^n and t^{n-1} respectively. It is assumed that $h_0^n(\mathbf{x}) = h_0$ constant in space and time because appropriate boundary conditions are assumed (see Section 2.2). We now insert (3.4) into the semi-discrete scheme (3.1)-(3.3) and retain the like powers of Fr. Inserting (3.4) into (3.3) and retaining the terms with Fr^{-2} and Fr^{-1} give formally

$$\nabla(h_0^{n+1} + z) = \nabla h_1^{n+1} = 0. \tag{3.5}$$

Now, inserting (3.4) into (3.1) and retaining the terms with Fr^0 lead to

$$\nabla\ .\ \Big((h_0U_0)^n - \frac{\Delta t}{2}\nabla\ .\ \big(\widehat{(h_0U_0)}^{n+\frac{1}{2}} \otimes \widehat{U_0}^{n+\frac{1}{2}}\big) - \frac{\Delta t}{2} h_0^{n+\frac{1}{2}} \nabla(h_2^{n+\frac{1}{2}} + z)\Big) = 0. \tag{3.6}$$

Now, inserting (3.4) into (3.3) and retaining the terms with Fr^0 lead to

$$(h_0U_0)^{n+1} = (h_0U_0)^n - \Delta t\nabla\ .\ \big(\widehat{(h_0U_0)}^{n+\frac{1}{2}} \otimes \widehat{U_0}^{n+\frac{1}{2}}\big) - \Delta t h_0^{n+\frac{1}{2}} \nabla(h_2^{n+\frac{1}{2}} + z). \tag{3.7}$$

From (3.7) one can deduce the following:

$$(h_0U_0)^n - \frac{\Delta t}{2}\nabla\ .\ \big(\widehat{(h_0U_0)}^{n+\frac{1}{2}} \otimes \widehat{U_0}^{n+\frac{1}{2}}\big) - \frac{\Delta t}{2} h_0^{n+\frac{1}{2}} \nabla(h_2^{n+\frac{1}{2}} + z) = \frac{(h_0U_0)^{n+1} + (h_0U_0)^n}{2}. \tag{3.8}$$

Hence, using (3.8), (3.6) becomes the following:

$$\nabla\ .\ \left(\frac{(h_0U_0)^{n+1} + (h_0U_0)^n}{2}\right) = 0 \Rightarrow \nabla\ .\ (h_0U_0)^{n+1} = 0. \tag{3.9}$$

In summary, the proposed semi-discrete numerical scheme yields the discrete limiting equations (3.5), (3.7) and (3.9) which are consistent approximations of the limiting system (2.17) as Fr $\to 0$. □

3.2. Fully-discrete numerical scheme

In what follows, we adopt a numerical strategy based on a finite volume method with cell-centered variables in order to discretize system (2.9). The domain Ω is divided using a uniform Cartesian grid, $\mathcal{C}(\Omega)$. Each cell $\mathcal{C}_{i,j} = (x_{i-\frac{1}{2}}, x_{i+\frac{1}{2}}) \times (y_{j-\frac{1}{2}}, y_{j+\frac{1}{2}})$, in the grid $\mathcal{C}(\Omega)$ is rectangular, whose sizes in the horizontal and vertical directions are respectively $\Delta x = x_{i+\frac{1}{2}} - x_{i-\frac{1}{2}}$ and $\Delta y = y_{j+\frac{1}{2}} - y_{j-\frac{1}{2}}$. The numerical unknowns are the approximation of the averaged value of the water height $h_{i,j}^n$ and of the velocity $U_{i,j}^n$ at the time t^n in each cell $\mathcal{C}_{i,j} \in \mathcal{C}(\Omega)$:

$$\psi_{i,j}^n \approx \frac{1}{\Delta x \Delta y} \iint\limits_{\mathcal{C}_{i,j}} \psi(x, y, t^n)\ \mathrm{d}x\mathrm{d}y.$$

Additionally, we use the following notations at the interface between cells $\mathcal{C}_{i,j}$ and $\mathcal{C}_{i+1,j}$:

$$\{\psi\}_{i+\frac{1}{2},j} = \frac{\psi_{i,j} + \psi_{i+1,j}}{2} \quad \text{and} \quad [\psi]_{i+\frac{1}{2},j} = \psi_{i+1,j} - \psi_{i,j}.$$

Similarly, we use the following notations at the interface between cells $\mathcal{C}_{i,j}$ and $\mathcal{C}_{i,j+1}$.

$$\{\psi\}_{i,j+\frac{1}{2}} = \frac{\psi_{i,j} + \psi_{i,j+1}}{2} \quad \text{and} \quad [\psi]_{i,j+\frac{1}{2}} = \psi_{i,j+1} - \psi_{i,j}.$$

The fully discrete numerical scheme of the water height conservation equation of system (2.9) reads as

$$h_{i,j}^{n+1} - h_{i,j}^{n} + \frac{\Delta t}{\Delta x}\Big(\mathcal{F}_{i+\frac{1}{2},j}^{n+\frac{1}{2}} - \mathcal{F}_{i-\frac{1}{2},j}^{n+\frac{1}{2}}\Big) + \frac{\Delta t}{\Delta y}\Big(\mathcal{F}_{i,j+\frac{1}{2}}^{n+\frac{1}{2}} - \mathcal{F}_{i,j-\frac{1}{2}}^{n+\frac{1}{2}}\Big) = 0, \tag{3.10}$$

with

$$\begin{aligned}\mathcal{F}_{i+\frac{1}{2},j}^{n+\frac{1}{2}} = \{(hu)^n\}_{i+\frac{1}{2},j} &- \frac{\Delta t}{2\Delta y}\Big(\{\widehat{(huv)}^{n+\frac{1}{2}}\}_{i+\frac{1}{2},j+\frac{1}{2}} - \{\widehat{(huv)}^{n+\frac{1}{2}}\}_{i+\frac{1}{2},j-\frac{1}{2}}\Big) \\ &- \frac{\Delta t}{2\Delta x}[\widehat{(hu^2)}^{n+\frac{1}{2}}]_{i+\frac{1}{2},j} - \frac{\Delta t}{2\Delta x \mathrm{Fr}^2}\{h^{n+\frac{1}{2}}\}_{i+\frac{1}{2},j}[\zeta^{n+\frac{1}{2}}]_{i+\frac{1}{2},j},\end{aligned} \tag{3.11}$$

and

$$\begin{aligned}\mathcal{F}_{i,j+\frac{1}{2}}^{n+\frac{1}{2}} = \{(hv)^n\}_{i,j+\frac{1}{2}} &- \frac{\Delta t}{2\Delta x}\Big(\{\widehat{(huv)}^{n+\frac{1}{2}}\}_{i+\frac{1}{2},j+\frac{1}{2}} - \{\widehat{(huv)}^{n+\frac{1}{2}}\}_{i-\frac{1}{2},j+\frac{1}{2}}\Big) \\ &- \frac{\Delta t}{2\Delta y}[\widehat{(hv^2)}^{n+\frac{1}{2}}]_{i,j+\frac{1}{2}} - \frac{\Delta t}{2\Delta y \mathrm{Fr}^2}\{h^{n+\frac{1}{2}}\}_{i,j+\frac{1}{2}}[\zeta^{n+\frac{1}{2}}]_{i,j+\frac{1}{2}},\end{aligned} \tag{3.12}$$

where

$$\{\psi\}_{i+\frac{1}{2},j+\frac{1}{2}} = \frac{\psi_{i,j} + \psi_{i+1,j} + \psi_{i,j+1} + \psi_{i+1,j+1}}{4}.$$

As proposed in [18], we consider here a centred approximation of the free surface in order to maintain the asymptotic limit. This also ensures the discrete stability of the steady-state at rest. The numerical scheme involves boundary conditions that vary according to the flow regime. In this study, we do not focus on the treatment of boundary condition (as it is well-known that handling boundary conditions for hyperbolic systems can be particularly challenging; for further information, see [22]). The scheme introduced in (3.10) is implicit and nonlinear with respect to the water height, thus one cannot solve it directly. To address this issue, the Newton-Raphson method is typically applied, converting the original nonlinear problem into a sequence of linear ones. Consequently, an iterative Newton process is employed at each time step to find the solution. Specifically, we define the scheme as $S_{i,j}(h^{n+1}) = 0$ with

$$S_{i,j}(h) = h_{i,j}^{n+1} - h_{i,j}^{n} + \frac{\Delta t}{\Delta x}\Big(\mathcal{F}_{i+\frac{1}{2},j}^{n+\frac{1}{2}} - \mathcal{F}_{i-\frac{1}{2},j}^{n+\frac{1}{2}}\Big) + \frac{\Delta t}{\Delta y}\Big(\mathcal{F}_{i,j+\frac{1}{2}}^{n+\frac{1}{2}} - \mathcal{F}_{i,j-\frac{1}{2}}^{n+\frac{1}{2}}\Big),$$

where the Newton method constructs a sequence $(h^{n,q})_{q\geq 0}$ initialized with $h^{n,0} = h^n$ and proceed as follows:

$$\begin{cases}\mathcal{J}\left(h^{n,q}\right)\delta_h^{n,q} = \mathcal{S}\left(h^{n,q}\right), \\ h^{n,q+1} = h^{n,q} - \delta_h^{n,q}.\end{cases}$$

In this context, $\mathcal{J}$ represents the Jacobian matrix of $S(h) = (S_{i,j}(h))_{\mathcal{C}_{i,j}\in\mathcal{C}(\Omega)}$. Moreover, h^{n+1} is defined as $\lim\limits_{q\to\infty} h^{n,q}$. A similar method based on Newton's approach is discussed in [11], where numerical results demonstrate quadratic convergence.

Once the water depth $h_{i,j}^{n+1}$ is recovered, the momentum balance is computed using the following

explicit upwind scheme with the extrapolation of the advection velocity:

$$
\begin{aligned}
&(hu)_{i,j}^{n+1} - (hu)_{i,j}^{n} \\
&+\frac{\Delta t}{\Delta x}\left(\widehat{u}_{i+\frac{1}{2},j}^{n+\frac{1}{2},W}\left(\{\widehat{hu}\}_{i+\frac{1}{2},j}^{n+\frac{1}{2}}\right)_{+} - \widehat{u}_{i+\frac{1}{2},j}^{n+\frac{1}{2},E}\left(\{\widehat{hu}\}_{i+\frac{1}{2},j}^{n+\frac{1}{2}}\right)_{-} - \widehat{u}_{i-\frac{1}{2},j}^{n+\frac{1}{2},W}\left(\{\widehat{hu}\}_{i-\frac{1}{2},j}^{n+\frac{1}{2}}\right)_{+} + \widehat{u}_{i-\frac{1}{2},j}^{n+\frac{1}{2},E}\left(\{\widehat{hu}\}_{i-\frac{1}{2},j}^{n+\frac{1}{2}}\right)_{-}\right) \\
&+\frac{\Delta t}{\Delta y}\left(\widehat{u}_{i,j+\frac{1}{2}}^{n+\frac{1}{2},S}\left(\{\widehat{hv}\}_{i,j+\frac{1}{2}}^{n+\frac{1}{2}}\right)_{+} - \widehat{u}_{i,j+\frac{1}{2}}^{n+\frac{1}{2},N}\left(\{\widehat{hv}\}_{i,j+\frac{1}{2}}^{n+\frac{1}{2}}\right)_{-} - \widehat{u}_{i,j-\frac{1}{2}}^{n+\frac{1}{2},S}\left(\{\widehat{hv}\}_{i,j-\frac{1}{2}}^{n+\frac{1}{2}}\right)_{+} + \widehat{u}_{i,j-\frac{1}{2}}^{n+\frac{1}{2},N}\left(\{\widehat{hv}\}_{i,j-\frac{1}{2}}^{n+\frac{1}{2}}\right)_{-}\right) \\
&\qquad = -\frac{\Delta t}{\Delta x} h_{i,j}^{n+\frac{1}{2}}\left(\{\zeta^{n+\frac{1}{2}}\}_{i+\frac{1}{2},j} - \{\zeta^{n+\frac{1}{2}}\}_{i-\frac{1}{2},j}\right),
\end{aligned}
\tag{3.13}
$$

$$
\begin{aligned}
&(hv)_{i,j}^{n+1} - (hv)_{i,j}^{n} \\
&+\frac{\Delta t}{\Delta y}\left(\widehat{v}_{i,j+\frac{1}{2}}^{n+\frac{1}{2},S}\left(\{\widehat{hv}\}_{i,j+\frac{1}{2}}^{n+\frac{1}{2}}\right)_{+} - \widehat{v}_{i,j+\frac{1}{2}}^{n+\frac{1}{2},N}\left(\{\widehat{hv}\}_{i,j+\frac{1}{2}}^{n+\frac{1}{2}}\right)_{-} - \widehat{v}_{i,j-\frac{1}{2}}^{n+\frac{1}{2},S}\left(\{\widehat{hv}\}_{i,j-\frac{1}{2}}^{n+\frac{1}{2}}\right)_{+} + \widehat{v}_{i,j-\frac{1}{2}}^{n+\frac{1}{2},N}\left(\{\widehat{hv}\}_{i,j-\frac{1}{2}}^{n+\frac{1}{2}}\right)_{-}\right) \\
&+\frac{\Delta t}{\Delta x}\left(\widehat{v}_{i+\frac{1}{2},j}^{n+\frac{1}{2},W}\left(\{\widehat{hu}\}_{i+\frac{1}{2},j}^{n+\frac{1}{2}}\right)_{+} - \widehat{v}_{i+\frac{1}{2},j}^{n+\frac{1}{2},E}\left(\{\widehat{hu}\}_{i+\frac{1}{2},j}^{n+\frac{1}{2}}\right)_{-} - \widehat{v}_{i-\frac{1}{2},j}^{n+\frac{1}{2},W}\left(\{\widehat{hu}\}_{i-\frac{1}{2},j}^{n+\frac{1}{2}}\right)_{+} + \widehat{v}_{i-\frac{1}{2},j}^{n+\frac{1}{2},E}\left(\{\widehat{hu}\}_{i-\frac{1}{2},j}^{n+\frac{1}{2}}\right)_{-}\right) \\
&\qquad = -\frac{\Delta t}{\Delta y} h_{i,j}^{n+\frac{1}{2}}\left(\{\zeta^{n+\frac{1}{2}}\}_{i,j+\frac{1}{2}} - \{\zeta^{n+\frac{1}{2}}\}_{i,j-\frac{1}{2}}\right),
\end{aligned}
\tag{3.14}
$$

with the positive and the negative part functions defined by $\psi_{\pm} = \dfrac{|\psi| \pm \psi}{2} \geq 0$. In line with [19], a centred scheme is employed to discretize the free surface ζ for any $\mathrm{Fr} > 0$. To formally achieve the second order space accuracy, the convective terms are treated using a MUSCL reconstruction [56] supplemented with a limiter to prevent the emergence of unwanted oscillations near discontinuous regions. For each cell $\mathcal{C}_{i,j}$, the reconstructed values at the interfaces are given by:

$$
\begin{aligned}
U_{i+\frac{1}{2},j}^{W} &= U_{i,j} + \frac{\Delta x}{2} \times \varphi\left(\frac{U_{i+1,j} - U_{i,j}}{\Delta x}, \frac{U_{i,j} - U_{i-1,j}}{\Delta x}\right), \\
U_{i-\frac{1}{2},j}^{E} &= U_{i,j} - \frac{\Delta x}{2} \times \varphi\left(\frac{U_{i+1,j} - U_{i,j}}{\Delta x}, \frac{U_{i,j} - U_{i-1,j}}{\Delta x}\right), \\
U_{i,j+\frac{1}{2}}^{S} &= U_{i,j} + \frac{\Delta y}{2} \times \varphi\left(\frac{U_{i,j+1} - U_{i,j}}{\Delta y}, \frac{U_{i,j} - U_{i,j-1}}{\Delta y}\right), \\
U_{i,j-\frac{1}{2}}^{N} &= U_{i,j} - \frac{\Delta y}{2} \times \varphi\left(\frac{U_{i,j+1} - U_{i,j}}{\Delta y}, \frac{U_{i,j} - U_{i,j-1}}{\Delta y}\right),
\end{aligned}
$$

where φ is a slope limiting function. In practice, we use the minmod limiting function [29] given by:

$$
\varphi(a,b) = \mathrm{minmod}(a,b) = \begin{cases} \min(a,b) & \text{if } a > 0 \text{ and } b > 0, \\ \max(a,b) & \text{if } a < 0 \text{ and } b < 0, \\ 0 & \text{otherwise.} \end{cases}
$$

The combination of space and time discretization in (3.10), (3.13) and (3.14) gives rise to a second-order ImEx scheme for the shallow water equations (2.9), referred to as ImEx 2.

In what follows, we provide the proof of the well-balanced property of the proposed ImEx 2 scheme, which ensures that the "lake at rest" steady-state solutions (2.8) are exactly preserved by the numerical method.

Theorem 2. *The ImEx 2 scheme* (3.10) *and* (3.13)-(3.14) *preserves the discrete steady-states at rest defined by* $U_{i,j}^{n} = 0$ *and* $\zeta_{i,j}^{n} = \zeta_0$.

Proof. Assuming the discrete unknowns at the nth time iteration satisfy the steady-state at rest, both the discharge and free surface variation vanish, i.e., $[\zeta^n]_{i+\frac{1}{2},j} = 0$ and $[\zeta^n]_{i,j+\frac{1}{2}} = 0$, hence the flux approximations (3.11) and (3.12) can be expressed as

$$\mathcal{F}^{n+\frac{1}{2}}_{i+\frac{1}{2},j} = -\frac{\Delta t}{2\Delta x \mathrm{Fr}^2}\{h^{n+\frac{1}{2}}\}_{i+\frac{1}{2},j}[\zeta^{n+1}]_{i+\frac{1}{2},j}, \tag{3.15}$$

and

$$\mathcal{F}^{n+\frac{1}{2}}_{i,j+\frac{1}{2}} = -\frac{\Delta t}{2\Delta y \mathrm{Fr}^2}\{h^{n+\frac{1}{2}}\}_{i,j+\frac{1}{2}}[\zeta^{n+1}]_{i,j+\frac{1}{2}}. \tag{3.16}$$

The fully discrete equation (3.10) for solving $h^{n+1}_{i,j}$ is first investigated. Substituting the discretizations (3.15) and (3.16) into (3.10), and since the free surface variations vanish, $[\zeta^n]_{i+\frac{1}{2},j} = [\zeta^n]_{i,j+\frac{1}{2}} = 0$, the scheme can be written as

$$\begin{aligned} h^{n+1}_{i,j} &- \frac{\Delta t^2}{2\Delta x^2 \mathrm{Fr}^2}\Big(\{h^{n+\frac{1}{2}}\}_{i+\frac{1}{2},j}[\zeta^{n+1}]_{i+\frac{1}{2},j} - \{h^{n+\frac{1}{2}}\}_{i-\frac{1}{2},j}[\zeta^{n+1}]_{i-\frac{1}{2},j}\Big) \\ &- \frac{\Delta t^2}{2\Delta y^2 \mathrm{Fr}^2}\Big(\{h^{n+\frac{1}{2}}\}_{i,j+\frac{1}{2}}[\zeta^{n+1}]_{i,j+\frac{1}{2}} - \{h^{n+\frac{1}{2}}\}_{i,j-\frac{1}{2}}[\zeta^{n+1}]_{i,j-\frac{1}{2}}\Big) \\ = h^n_{i,j} &- \frac{\Delta t^2}{2\Delta x^2 \mathrm{Fr}^2}\Big(\{h^{n+\frac{1}{2}}\}_{i+\frac{1}{2},j}[\zeta^{n}]_{i+\frac{1}{2},j} - \{h^{n+\frac{1}{2}}\}_{i-\frac{1}{2},j}[\zeta^{n}]_{i-\frac{1}{2},j}\Big) \\ &- \frac{\Delta t^2}{2\Delta y^2 \mathrm{Fr}^2}\Big(\{h^{n+\frac{1}{2}}\}_{i,j+\frac{1}{2}}[\zeta^{n}]_{i,j+\frac{1}{2}} - \{h^{n+\frac{1}{2}}\}_{i,j-\frac{1}{2}}[\zeta^{n}]_{i,j-\frac{1}{2}}\Big). \end{aligned}$$

The unique solution is $h^{n+1}_{i,j} = h^n_{i,j}$, which implies $\zeta^{n+1}_{i,j} = \zeta_0$.

Finally, since $\zeta^{n+1}_{i,j} = \zeta^n_{i,j} = \zeta_0$, the right hand side terms in (3.13) and (3.14) vanish, and thus we get that:

$$\begin{aligned} (hu)^{n+1}_{i,j} &= (hu)^n_{i,j} = 0, \\ (hv)^{n+1}_{i,j} &= (hv)^n_{i,j} = 0. \end{aligned}$$

In summary, when considering the "lake at rest" steady-state solutions, the proposed fully discrete numerical scheme yields $U^{n+1}_{i,j} = 0$ and $\zeta^{n+1}_{i,j} = \zeta_0$, thereby justifying the well-balanced property of the developed numerical methods. □

4. Test cases

This section presents a series of numerical test cases in both one-dimensional and two-dimensional settings to assess the performance of the proposed ImEx 2 numerical scheme. The one-dimensional tests begin with demonstrations of the scheme's second-order accuracy using a moving manufactured solution and a stationary subcritical solution. This is followed by an evaluation of its shock-capturing capabilities through the computation of a steady transcritical solution featuring a shock. Next, a classical Riemann problem is examined, and a low Froude number gravity wave simulation is conducted to highlight the advantages of the ImEx 2 scheme over the reference second-order explicit scheme from [46], particularly in low Froude number flows.

In the two-dimensional setting, three numerical experiments are proposed: one steady-state and two time-dependent cases, involving both flat and uneven bottom topographies. The first test investigates a 2D cylindrical explosion problem, showcasing the ImEx 2 scheme's superior performance in capturing the limit solution in low Froude number flows compared to the reference explicit scheme. The second test focuses on a specific member of the family of 2D non-trivial steady-state solutions over variable topography, demonstrating the robustness of the well-balanced discretization and boundary treatments. Finally, the third test examines a traveling vortex over a flat topography, verifying the second-order accuracy of the ImEx 2 scheme in the low Froude number regime and highlighting its significant computational efficiency relative to the reference explicit scheme.

In all numerical simulations, the time step is governed by the CFL condition associated with the first-order Implicit-Explicit Centered Potential Regularization (ImEx CPR) scheme introduced in [50]. At the interface between cells $\mathcal{C}_{i,j}$ and $\mathcal{C}_{i+1,j}$, this condition is expressed as follows:

$$\left(|\{h^{n+1}u^n\}_{i+\frac{1}{2},j}| + \{h^{n+1}\}_{i+\frac{1}{2},j}\sqrt{\frac{\gamma}{4}\frac{|[\zeta^{n+1}]_{i+\frac{1}{2},j}|}{\mathrm{Fr}^2}}\right)\Delta t \leq \min(h_{i,j}^{n+1}, h_{i+1,j}^{n+1})\frac{\Delta x}{8},$$

where γ is a regularization parameter set to 1. The time step is determined as the minimum value satisfying this condition across all cell interfaces.

4.1. 1D Numerical tests

4.1.1. Manufactured solution

In this test case, we verify the second-order accuracy of the proposed ImEx 2 scheme using a moving manufactured solution. To this end, we consider the following one-dimensional non linear shallow water equations in the flat bottom case ($z = 0$):

$$\begin{cases}\partial_t h + \partial_x(hu) = 0,\\ \partial_t(hu) + \partial_x\left(hu^2 + g\frac{h^2}{2}\right) = \Phi.\end{cases} \tag{4.1}$$

We construct the source term $\Phi = \Phi(x,t)$ in order to impose the solution to be equal to

$$\begin{cases} h_{ex}(x,t) = h_0 + a\ \mathrm{sech}^2(\kappa(x - x_0 - ct))\ ,\\ u_{ex}(x,t) = c\Big(1 - \dfrac{h_0}{h_{ex}(x,t)}\Big)\ ,\\ \kappa = \dfrac{\sqrt{3a}}{2h_0\sqrt{h_0+a}}, \quad c = \sqrt{g(h_0+a)}. \end{cases} \tag{4.2}$$

Following the classical manufactured solution method, we set

$$\begin{aligned}\Phi(x,t) &= \partial_t(h_{ex}(x,t)u_{ex}(x,t)) + \partial_x\Big(h_{ex}(x,t)u_{ex}^2(x,t) + g\frac{h_{ex}^2(x,t)}{2}\Big)\\ &= h_{ex}(\partial_t u_{ex} + u_{ex}\partial_x u_{ex} + g\partial_x h_{ex}).\end{aligned}$$

The initial condition is given by the exact solution at time $t = 0$ on the domain $\Omega = [0, 50]$ with $a = 1.2$, $h_0 = 1$, $x_0 = 15$ and $g = 9.81$. We set Dirichlet boundary conditions given by the exact solution at the borders of the domain. In Figure 2, we plot in a log-log scale the L^1-errors for h and hu as a function of the space step Δx. One can clearly see that the theoretical second-order rate of convergence is validated numerically.

4.1.2. Moving steady-states

We will now evaluate the scheme's capacity to maintain steady-states with a nonzero discharge. Two experiments, based on Goutal and Maurel's test cases [31], are conducted: one for subcritical flow and another for transcritical flow with a shock. In the one-dimensional case, the system of equations (2.7) reduces to the following Bernoulli relation:

$$\frac{q_0^2}{2h^2} + g(h + z) = H \tag{4.3}$$

where q_0 represents the constant discharge and H denotes the total head, which is calculated using known values from the upstream boundary of the domain. In the case of transcritical flow, a stationary shock is present; while the discharge remains constant, the total head exhibits a discontinuity at the shock's location.

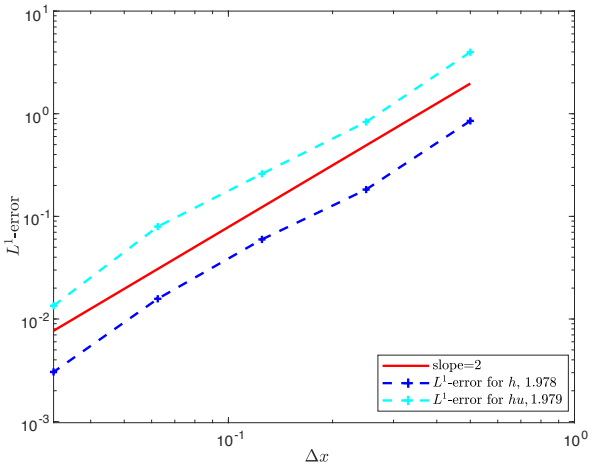

Figure 2: Manufactured solution: L^1-errors of the ImEx 2 scheme for h and hu as a function of Δx.

Subcritical flow. In this test case, we verify the second-order accuracy of the proposed ImEx 2 scheme using a stationary subcritical solution. The computational domain is $[0, 25]$, and the topography features a bump, defined as follows:

$$z(x) = \begin{cases} 0.2 - 0.05(x-10)^2 & \text{if } 8 < x < 12, \\ 0 & \text{otherwise.} \end{cases}$$

We use the following initial conditions $h(x,0)+z(x) = 2$ and $h(x,0)u(x,0) = 0$. We have $h(0,t)u(0,t) = 4.42$ and $h(25,t) = 2$ as boundary conditions. Now, we define a global relative change indicator to evaluate whether a numerical steady-state solution has been achieved. This indicator, first introduced in [43], indicates convergence when its value, denoted as R and given by (4.4), falls below a specified threshold R_c ($R_c \to 0$). For this particular test case, we set $R_c = 10^{-9}$. It is important to note that the convergence referenced here pertains to a numerical steady-state rather than a physical one, owing to the influence of numerical errors.

$$R = \sqrt{\sum_{i=1}^{N} \left(\frac{h_i^{n+1} - h_i^n}{h_i^n} \right)^2}, \tag{4.4}$$

where N represents the total number of grid cells, and the superscripts n and $n+1$ denote consecutive time steps. In Figure 3, we present the results obtained using the ImEx 2 scheme with 800 grid cells. A strong agreement is observed between the numerical solutions and the exact ones obtained using (4.3). This is further supported by Figure 4, which reports the L^1-errors for both h and hu, confirming second-order accuracy.

Transcritical with shock. This test case is devoted to a transcritical flow with a shock where we analyze the shock-capturing capability of the proposed ImEx 2 scheme. Using the same simulation domain, bottom topography, and R_c as those in the previous test case, we consider the following initial data:

$$h(x,0) + z(x) = 0.33 \quad \text{and} \quad h(x,0)u(x,0) = 0.$$

We impose $h(0,t)u(0,t) = 0.18$ at the left end of the domain and $h(25,t) = 0.33$ at the right end. The domain is discretized using 200 grid cells. The exact solution is obtained using (4.3), where in the case of a transcritical flow, a stationary shock is present; although the discharge remains constant, the total head, as described by the Bernoulli equation (4.3), exhibits a discontinuity at the shock's location. In Figure 5, we present a comparison between the results from the ImEx 2 scheme and the first-order Implicit Explicit Centered Potential Regularization (ImEx CPR) scheme developed in [50]. The numerical solutions show a strong agreement with the exact ones. Additionally, it is evident from

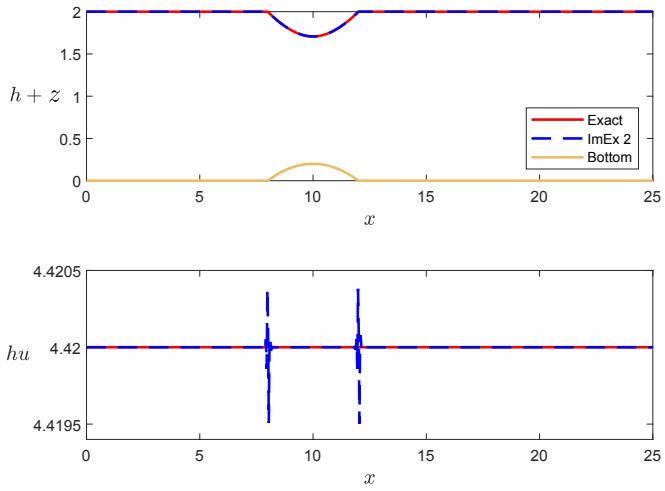

Figure 3: Subcritical solution: comparison of numerical (with $N = 800$ grid cells) and exact solutions. Top: free surface elevation, bottom: discharge.

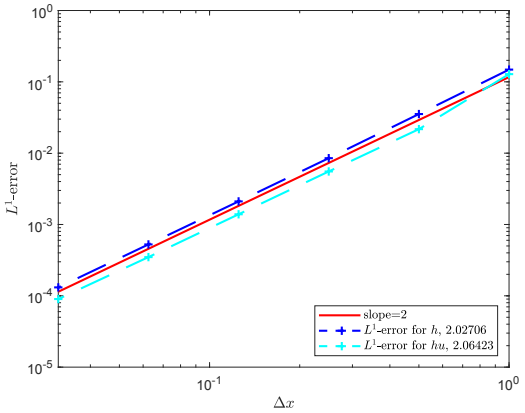

Figure 4: Subcritical solution: L^1-errors of the ImEx 2 scheme for h and hu as a function of Δx.

the flow discharge figure that the second-order ImEx 2 scheme yields a more accurate solution compared to the ImEx CPR scheme. It can be noted that the L^1-error of the discharge is very low, being of the order 8.7×10^{-3} while the error of the discharge obtained with the ImEx CPR scheme is three times larger of the order 2.66×10^{-2}.

4.1.3. Riemann problem

We now apply the ImEx 2 scheme to a 1D shock tube test case, with a spatial domain defined as $[0, 1]$. The initial conditions are given by:

$$h(x,0) = \begin{cases} 1+\varepsilon & \text{if } x < 0.5, \\ 1 & \text{otherwise;} \end{cases} \qquad h(x,0)u(x,0) = 1.$$

Homogeneous Neumann boundary conditions are imposed at both ends of the domain. The exact solution of this Riemann problem features a leftward-propagating rarefaction wave and a rightward-moving shock wave. In Figure 6, we compare the performance of the ImEx 2 scheme and the ImEx CPR scheme for different values of the squared Froude number, ε. The left panel shows the results for $\varepsilon = 1$ using 50 discretization cells at $t_f = 0.125$ s, while the right panel presents the results for $\varepsilon = 10^{-2}$ using 125 discretization cells at $t_f = 2 \times 10^{-2}$ s. As expected, the first-order CPR scheme (solid blue line) introduces substantial diffusion, whereas the second-order ImEx 2 scheme (red dashed line) delivers a more accurate capture of intermediate states. Nonetheless, overshoots and undershoots appear at the front and rear of the rarefaction wave and around the shock wave when the Froude

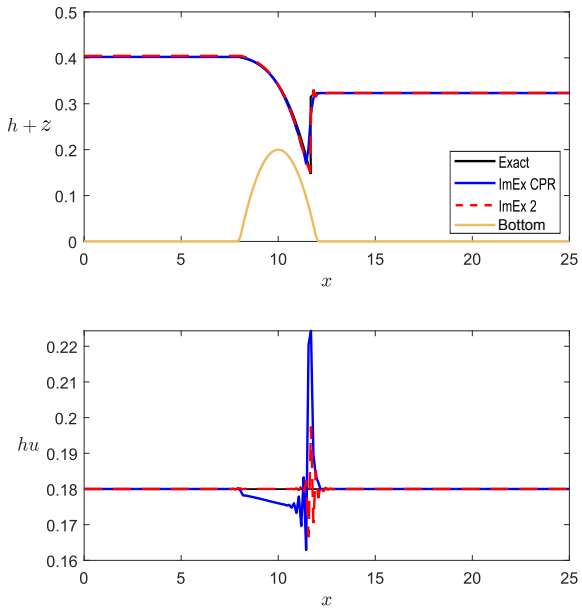

Figure 5: Transcritical flow with a shock: comparison of the ImEx 2 and the ImEx CPR schemes.

number decreases. As noted in [21], second-order implicit-explicit time discretizations for this class of problems face similar challenges as traditional implicit schemes for hyperbolic problems of order higher than one [30], particularly the loss of the total variation diminishing (TVD) property. The oscillations in the second-order ImEx 2 scheme arise from the time discretization, indicating the need for a limiter. However, addressing this issue is beyond the scope of this paper and is left for a future work. One can see [21] where an increase in precision was achieved by introducing a new paradigm of implicit time integrator by coupling first-order in time schemes with second-order ones in the same spirit as highly accurate shock-capturing TVD methods in space.

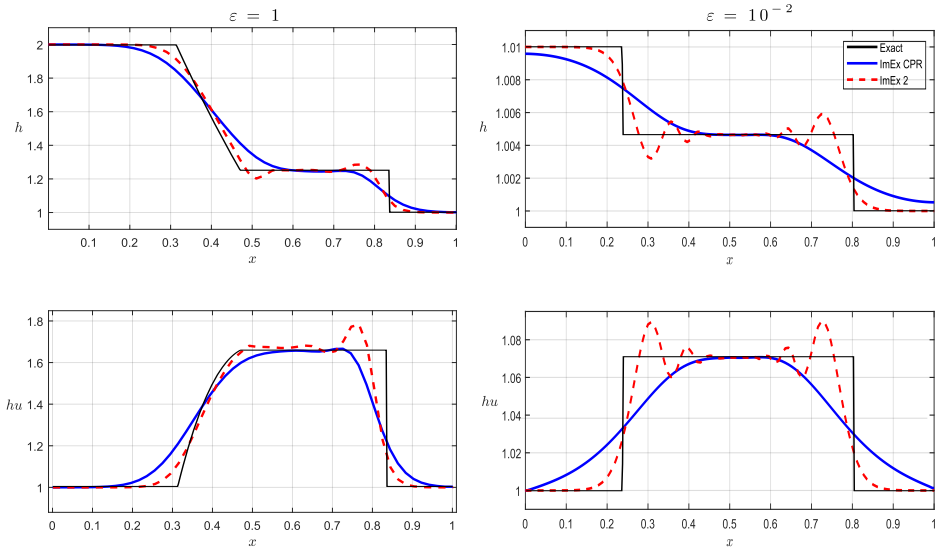

Figure 6: Riemann problem: comparison of the ImEx 2 and the ImEx CPR schemes. (Left) $\varepsilon = 1$, 50 discretization cells and $t_f = 0.125$ s; (right) $\varepsilon = 10^{-2}$, 125 discretization cells and $t_f = 2 \times 10^{-2}$ s.

4.1.4. Low Froude number gravity wave

One of the main advantages of ImEx schemes over traditional explicit methods is their ability to accommodate larger time steps, making them particularly efficient for simulating low Froude number flows. To demonstrate this efficiency, we examine a low Froude number gravity wave simulation inspired by [23]. The computational domain is $\Omega = [x_L, x_R]$, with initial conditions $h(x,0) = h_0$ and $u(x,0) = 0$. The bottom is flat ($z = 0$), and boundary conditions are specified as follows: a no-flux condition $u(x_L,t) = 0$ on the left boundary, and a periodic water height signal at the right boundary, given by $h(x_R,t) = h_0 + A_h \sin\left(\frac{2\pi t}{T}\right)$. For this problem, we use the parameters $x_L = 0$, $x_R = 100\,\text{km}$, $h_0 = 100\,\text{m}$, $A_h = 5\,\text{m}$, and a tidal period $T = 12\,\text{h}$. Simulations are conducted with the ImEx 2 scheme and the HLL-MUSCL-RK2 explicit scheme from [46] both using 100 cells. The results are compared to a solution obtained from [23] using the semi-implicit DG scheme with a polynomial basis of degree 5 and 200 cells. The final simulation time is $t = 96\,\text{h}$ with results showing the temporal evolution of water height h and velocity u at $x = 25$ km, as illustrated in Figure 7. In this simulation, the maximum Froude number is $\text{Fr}_{\max} = 0.016$. Comparatively, the ImEx 2 scheme solution aligns more closely with the semi-implicit DG solution than the HLL-MUSCL-RK2 solution. Additionally, the ImEx 2 scheme requires only 1.5 seconds of CPU time to complete the simulation up to the final time $t = 96\,\text{h}$, versus 42.2 seconds for the explicit HLL-MUSCL-RK2 scheme, underscoring the computational efficiency of the ImEx 2 scheme in low Froude number flows.

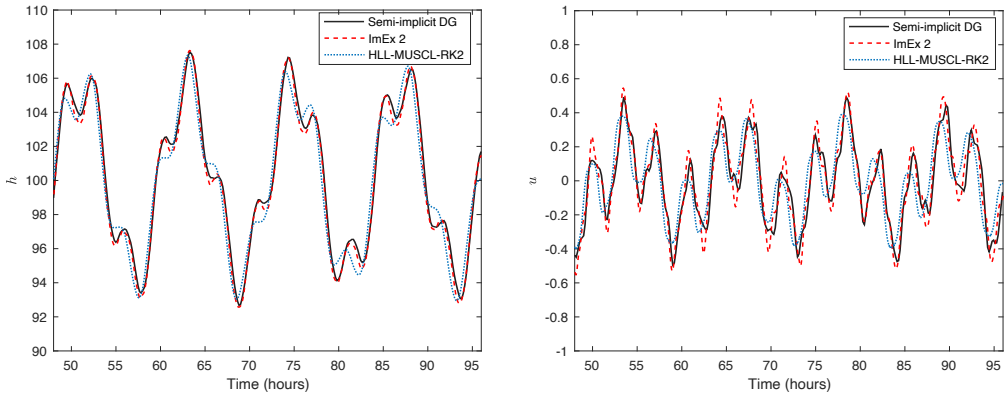

Figure 7: Low Froude gravity wave: comparison of the ImEx 2 and the HLL-MUSCL-RK2 schemes with the reference solution at $x = 25$ km. (Left) water height h ; (right) velocity u.

4.2. 2D Numerical test

4.2.1. 2D cylindrical explosion problem

In this test case, we evaluate the performance of the ImEx 2 scheme on non-steady solutions for small Froude numbers. Inspired by studies on the 2D cylindrical explosion problem for the isentropic Euler system in [20, 7], we adapt the test to the homogeneous shallow water equations (2.1). These equations share a similar mathematical structure with the isentropic Euler equations when the water depth h is analogous to the gas density ρ, and the equation of state for compressible gas is defined as $p(\rho) := \frac{1}{2}\rho^2$.

The computational domain is set to be $[-1,1] \times [-1,1]$, with an initial water depth defined as:

$$h(x,y,0) = \begin{cases} 1 + Fr^2, & \text{if } r^2 \le 1/4, \\ \\ 0, & \text{otherwise,} \end{cases}$$

where $r = \sqrt{x^2 + y^2}$ denotes the radial distance. The initial velocity components are given by:

$$u(x,y,0) = -\frac{\alpha(x,y)}{h(x,y,0)}\frac{x}{r}, \quad v(x,y,0) = -\frac{\alpha(x,y)}{h(x,y,0)}\frac{y}{r},$$

where $\alpha(x,y) = \max(0, 1-r)(1 - \exp(-16r^2))$. For $r \le 10^{-15}$, both u and v are set to zero. The initial data are represented in Figure 8. Periodic boundary conditions are applied, and the computational grid

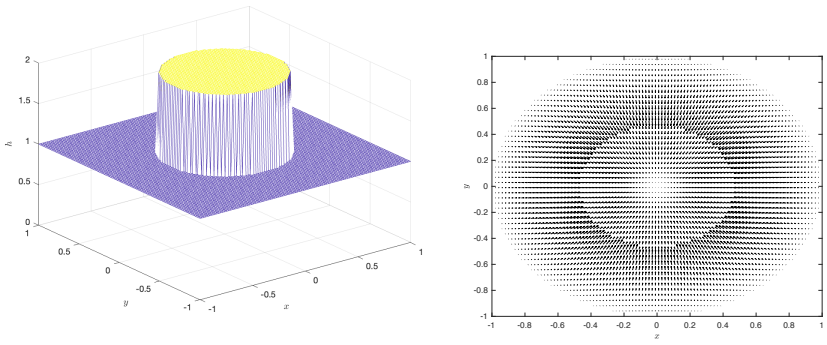

Figure 8: 2D cylindrical explosion, Fr = 1: Initial water depth (left), and two dimensional velocity field (right).

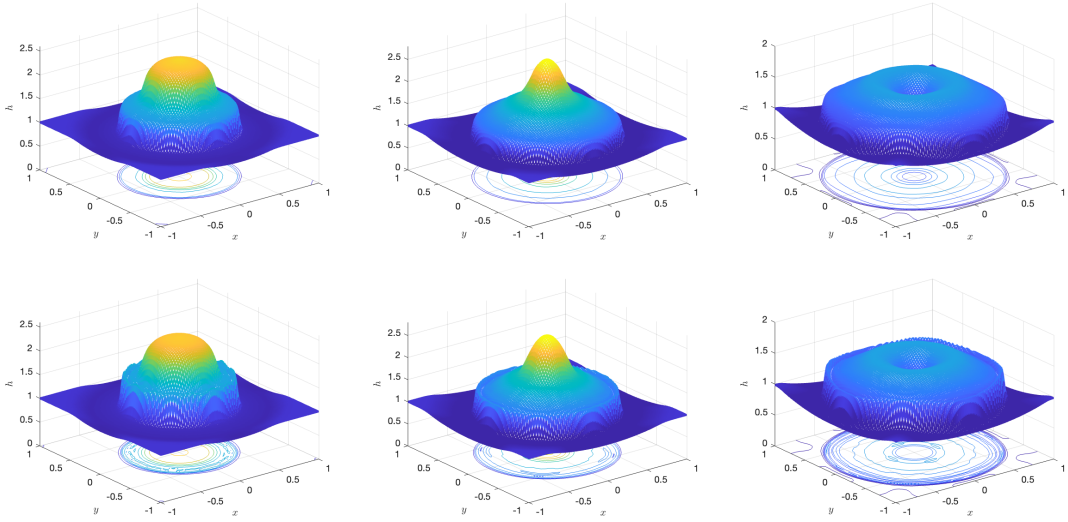

Figure 9: 2D cylindrical explosion, Fr = 1: $t = 0.1$ (left panel), $t = 0.24$ (middle panel), and $t = 0.4$ (right panel). Top images show the water depth profile for the HLL-MUSCL-RK2 scheme. Bottom images show the water depth profile for the ImEx 2 scheme.

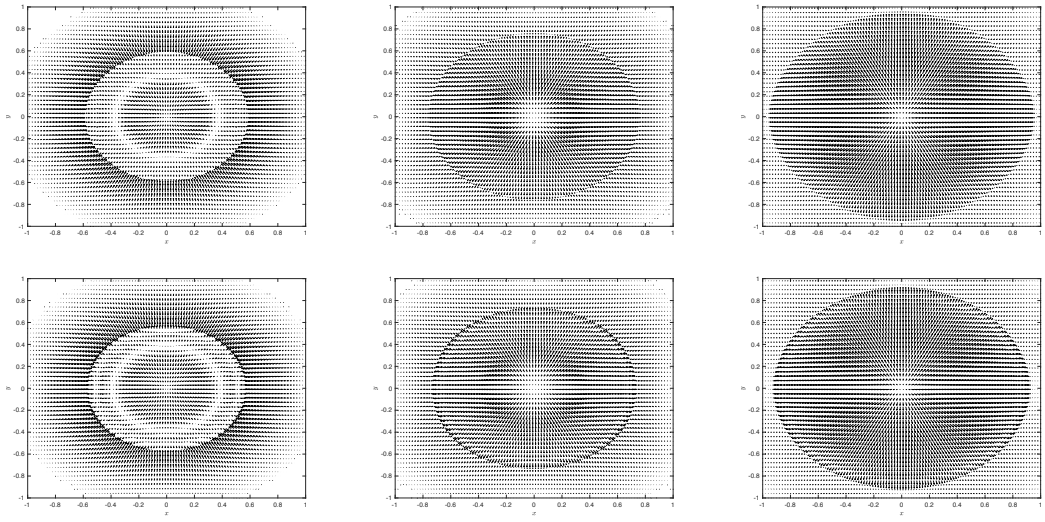

Figure 10: 2D cylindrical explosion, Fr = 1: $t = 0.1$ (left panel), $t = 0.24$ (middle panel), and $t = 0.4$ (right panel). Top images show the velocity field for the HLL-MUSCL-RK2 scheme. Bottom images show the velocity field for the ImEx 2 scheme.

consists of 100 cells in each direction. We compute the solution for various Froude numbers (Fr = 1 and Fr = 10^{-2}) using both the ImEx 2 scheme and the HLL-MUSCL-RK2 explicit scheme. Figures 9-10 illustrate the water depth and the velocity field for Fr = 1 at different times $t = 0.1, 0.24, 0.4$, comparing results from both schemes. These figures confirm that the ImEx 2 scheme accurately replicates the numerical behaviour of the explicit scheme at the Froude number Fr = 1. For the low Froude number case (Fr = 10^{-2}), Figure 11 displays the water depth, velocity field, and divergence of the velocity field at $t = 0.145$. The results show that the ImEx 2 scheme effectively captures the limit solution, whereas the explicit scheme continues to resolve small wave dynamics. Notably, the water depth deviation in the ImEx 2 scheme is of the order $\mathcal{O}(\text{Fr}^2)$ (approximately 10^{-4}), and the divergence of the velocity field is around 10^{-2}. These observations confirm the ImEx 2 scheme's capability to accurately handle low Froude number flows. From a computational perspective, the ImEx 2 scheme demonstrates significant efficiency, requiring approximately three times less computational cost than the explicit scheme in our implementation.

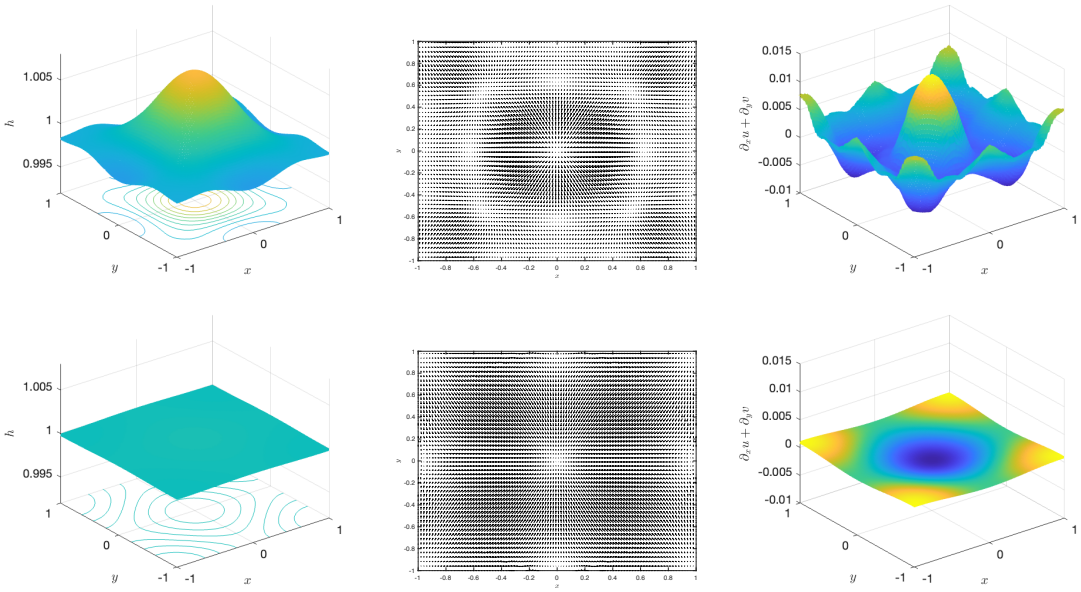

Figure 11: 2D cylindrical explosion, Fr = 10^{-2} at $t = 0.145$: water depth profile (left panel), velocity field (middle panel), and divergence of the velocity field (right panel). Top images for the HLL-MUSCL-RK2 scheme. Bottom images for the ImEx 2 scheme.

4.2.2. 2D potential solution with variable topography

To assess the well-balanced discretization and the proposed boundary treatment, we examine a specific case from the family of 2D exact solutions presented in [52], which satisfies non-trivial steady-state conditions. On the spatial domain $[-1, 1] \times [-1, 1]$, we use a solution where the velocity field is divergence-free and derived from the harmonic function $\psi = xy$, leading to the velocity components $u = \dfrac{\partial \psi}{\partial y} = x, v = \dfrac{\partial \psi}{\partial x} = y$. The relative water height is defined as $h = \alpha + \psi$, while the bed elevation $z(x, y)$ is calculated from $g(h + z(x, y)) = 30 - \dfrac{x^2 + y^2}{2}$. For this test case, we set $\alpha = 1.5$ and use a gravitational acceleration $g = 10$. The boundary conditions specify subcritical inlets at the top and bottom boundaries, and subcritical outlets at the left and right boundaries, since the Froude number remains below one throughout the domain. Starting from the exact solution, we evolve the system towards a steady-state using the ImEx 2 scheme. In Figure 12, we provide a three-dimensional representation of the steady-state solution, which includes the topography. We also plot the Froude number $\text{Fr} = \sqrt{\dfrac{u^2 + v^2}{gh}}$ over the domain. Additionally, we compare the analytical and numerical solutions for the height h. The numerical results were derived using the ImEx 2 scheme on a 100×100 grid resolution.

The comparison demonstrates a strong agreement between the numerical and exact solutions across all state variables.

Now, we repeat the same test case but in a smaller Froude number regime. To this end, we only change the value of α, we consider $\alpha = 150$ in the definition of h. As a result, the Froude number does not exceed 0.0370. In Figure 13, we present the three-dimensional representation of the steady-state solution for the smaller Froude number regime (with $\alpha = 150$). The plot includes the water height, the topography and a visualization of the Froude number across the domain, where values remain significantly below 0.0370. A comparison between the analytical and numerical solutions for the height h shows an excellent agreement, demonstrating the robustness of the method in handling low Froude number flows.

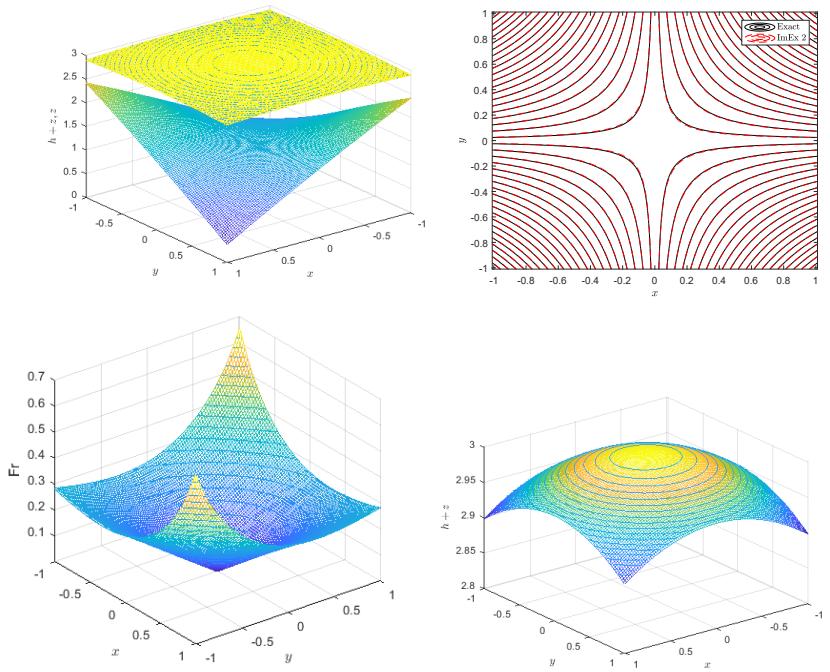

Figure 12: 2D potential solution, $\alpha = 1.5$: 3D view (top left), contour plot for h (top right) and Froude number Fr (bottom left) and free surface level $\zeta = h + z$ (bottom right).

4.2.3. Traveling vortex

In [53], a solution to the two-dimensional shallow water equations is derived for traveling vortex scenarios. The problem is set within a unit square domain $[0, 1] \times [0, 1]$, where periodic boundaries are enforced along the x-axis, and absorbing boundaries are applied along the y-axis. The initial setup for this configuration, depicted in Figure 14, is given by the following conditions:

$$h(x, y, 0) = 10 + \begin{cases} \left(\frac{\varepsilon\Gamma}{\omega}\right)^2 (\phi(\omega r_c) - \phi(\pi)), & \text{if } \omega r_c \leq \pi, \\ 0, & \text{otherwise,} \end{cases}$$

$$u(x, y, 0) = 6 + \begin{cases} \Gamma(1 + \cos(\omega r_c))(0.5 - y), & \text{if } \omega r_c \leq \pi, \\ 0, & \text{otherwise,} \end{cases}$$

$$v(x, y, 0) = \begin{cases} \Gamma(1 + \cos(\omega r_c))(x - 0.5), & \text{if } \omega r_c \leq \pi, \\ 0, & \text{otherwise,} \end{cases}$$

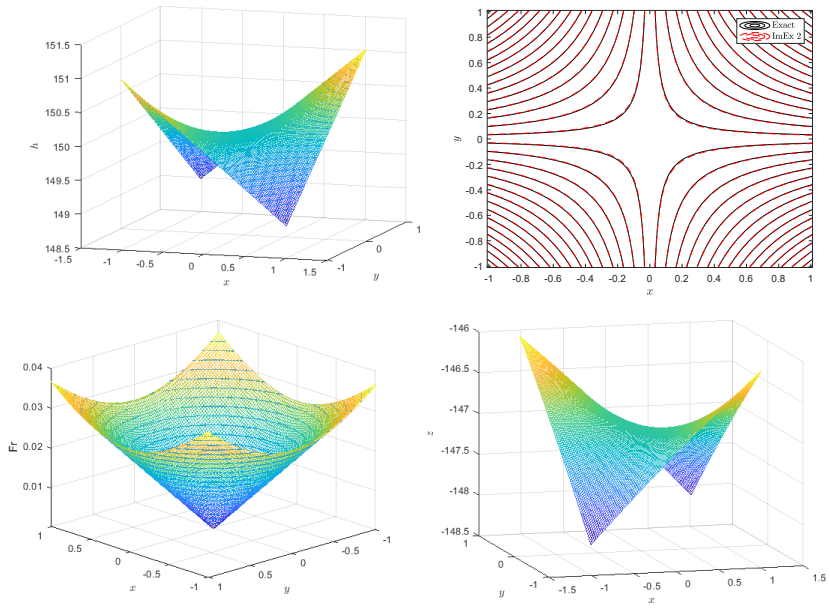

Figure 13: 2D potential solution, $\alpha = 150$: water height h (top left), contour plot for h (top right) and Froude number Fr (bottom left) and bottom topography z (bottom right).

$$r_c = \|(x, y) - (0.5, 0.5)\|, \ \Gamma = 15, \ \omega = 4\pi,$$
$$\phi(r) = 2\cos(r) + 2rsin(r) + \frac{1}{8}\cos(2r) + \frac{r}{4}\sin(2r) + \frac{3}{4}r^2.$$

A vortex initially located at $(0.5, 0.5)$ undergoes rotational motion and is repeatedly carried to the right with a period $T = 1/6$ by a uniform flow with an advection velocity of $U_{ref} = (6, 0)$. The Froude number is determined by modifying ε, where $\text{Fr} = \dfrac{u_{ref}}{h_{ref}} = \dfrac{6\varepsilon}{\sqrt{10}}$. Figure 15 illustrates a comparison between results obtained using the ImEx 2 scheme and the second-order explicit scheme (HLL-MUSCL-RK2) for two Froude numbers: $\text{Fr} = 1$ (top) and $\text{Fr} = 10^{-3}$ (bottom), with a grid resolution of 200×200. The numerical solutions are compared against the exact ones using contour plots of the depth h (left) and cross-sections at $y = 0$ (right), at the moment when the vortex returns to its starting location at time $T = 1/6$. For $\text{Fr} = 1$, both schemes yield results that are virtually indistinguishable from the exact solution. However, for the lower Froude number $\text{Fr} = 10^{-3}$, noticeable differences arise between the two schemes, as seen in the bottom plots of Figure 15. On this grid, the ImEx 2 scheme shows a clear advantage, with the explicit scheme exhibiting greater numerical diffusion, particularly in low Froude number scenarios. The results confirm that the ImEx 2 scheme accurately preserves both the vortex's position and amplitude across different flow conditions.

Table 1 presents the L^1-error measurements for the primitive variables h, hu, and hv, along with the EOC for the ImEx 2 scheme, using various grid resolutions $N \times N$. The numerical solutions and exact solutions are obtained at time $T = 1/6$ for different Froude numbers: $\text{Fr} = 1, 0.1, 0.01$, and 0.001. The results confirm that the ImEx 2 scheme achieves second-order accuracy across the range of Froude numbers tested.

In Figure 16, the L^1-errors for h are shown for both the explicit HLL-MUSCL-RK2 scheme and the ImEx 2 scheme, plotted against the grid size on a log-log scale. Additionally, a solid line with a slope of 2 and a dashed line with a slope of 1 are included for reference. For $\text{Fr} = 1$ (left), the results confirm that both schemes exhibit second-order convergence as expected. However, when $\text{Fr} = 10^{-3}$ is used, the explicit scheme experiences a reduction in its convergence order, while the ImEx 2 scheme remains unaffected by the scaling parameter.

It is useful to compare the CPU times required by the ImEx 2 scheme and the explicit HLL-MUSCL-RK2 scheme. These timings are presented in Table 2, where significant computational savings for the ImEx 2 scheme in the low Froude number regime are clearly evident.

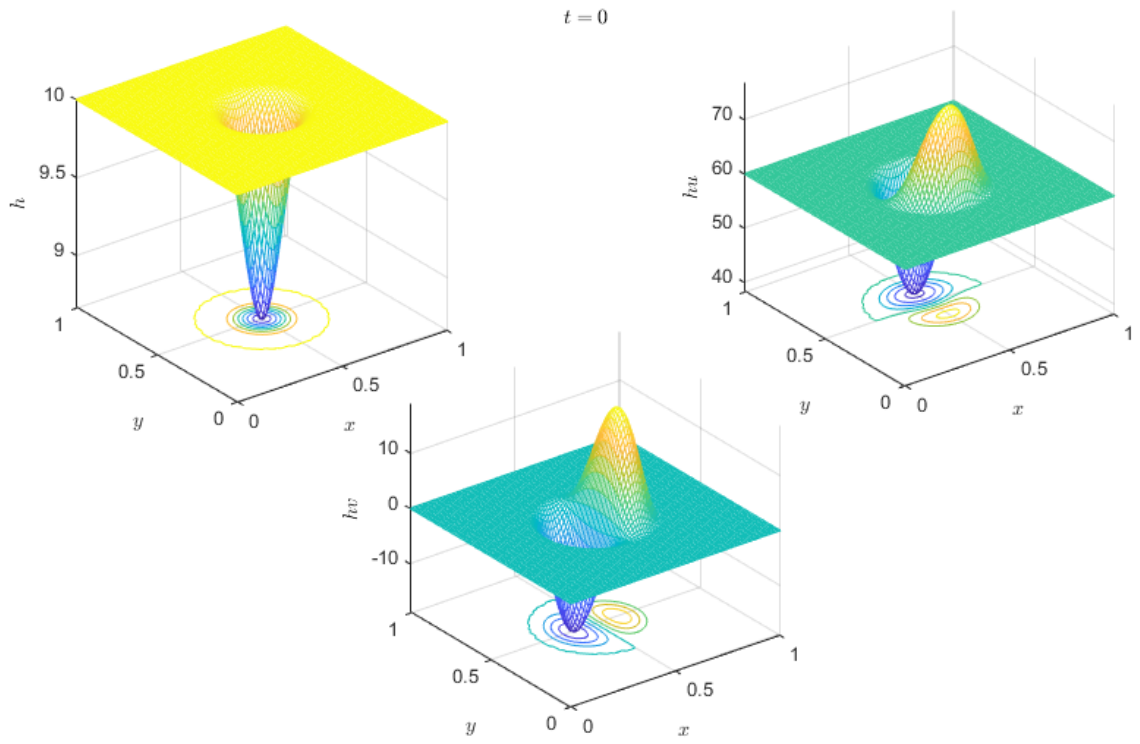

Figure 14: Traveling vortex: initial condition with Fr = 1, computed on the 80 × 80 grid.

5. Conclusion

We developed a novel numerical method specifically designed for shallow water flows at low Froude numbers addressing the scientific challenges in this regime. As the Froude number approaches zero, the hyperbolic nature of the governing equations changes, introducing stiffness that imposes restrictive CFL conditions and increases computational cost. To overcome these difficulties, we proposed a second-order implicit-explicit (ImEx) scheme capable of efficiently handling a full range of Froude numbers. In this approach, the water height and hybrid mass fluxes are computed implicitly, while the velocity is treated explicitly. A Crank-Nicolson scheme is employed to achieve second-order accuracy while minimizing the number of required linear system solutions, thereby enhancing computational efficiency. The developed scheme is asymptotic preserving in the sense that it provides consistent and stable approximation of the underlying system in the low Froude number regime and also guarantees the well-balanced property. The scheme has been validated against various numerical test cases, both in one and two horizontal dimensions. We proved the accuracy of the model using both steady and unsteady flows and used numerical test cases on a wide range of Froude numbers which are related with coastal and oceanic applications. We compared the CPU time of our scheme to that of a classical HLL-MUSCL-RK explicit scheme using three test cases: a low Froude gravity wave, a 2D cylindrical explosion and a 2D traveling vortex. Our results show that our method can be more than 20 times faster on large meshes and low Froude numbers.

Acknowledgement

The authors acknowledge the financial support of the ANR-21-CE46-0004 LAGOON project.

In memoriam

This paper is dedicated to the memory of Prof. Arturo Hidalgo López (*July 03$^{\text{rd}}$ 1966 - †August 26$^{\text{th}}$ 2024) of the Universidad Politecnica de Madrid, organizer of HONOM 2019 and active participant in

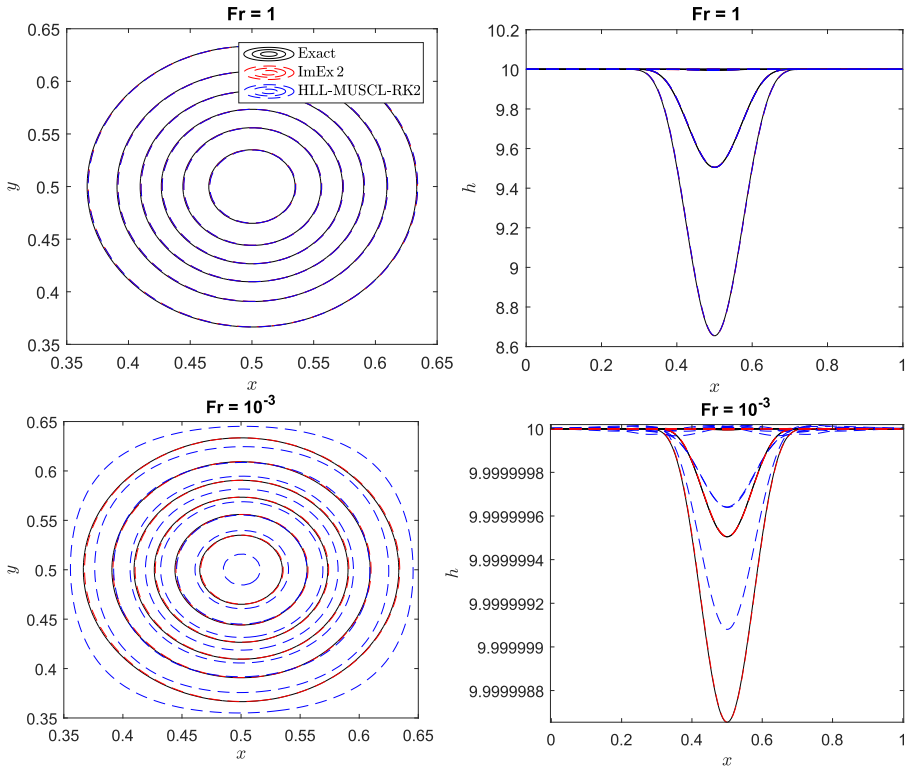

Figure 15: Traveling vortex: comparison of the contour plots for h (left) and at $y = 0$ (right) at $T = 1/6$ of the explicit HLL-MUSCL-RK2 scheme and the ImEx2 scheme with $\mathrm{Fr} = 1$ (top) and $\mathrm{Fr} = 10^{-3}$ (bottom), computed on the 200×200 grid.

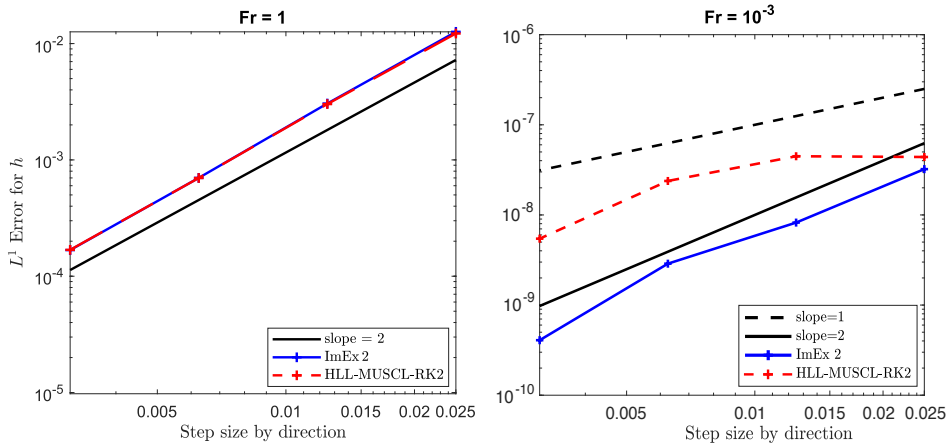

Figure 16: Traveling vortex: comparison of the L^1-errors for h of the explicit HLL-MUSCL-RK2 scheme and the ImEx2 scheme with $\mathrm{Fr} = 1$ and $\mathrm{Fr} = 10^{-3}$.

many other editions of HONOM. Our thoughts and wishes go to his wife Lourdes and his sister María Jesús, whom he left behind.

Fr = 1, $T = 1/6$

N	L^1-error in h	EOC	L^1-error in hu	EOC	L^1-error in hv	EOC
40	1.262e-02		2.497e-01		4.027e-01	
80	3.0520e-03	2.0474	7.070e-02	1.8206	1.259e-01	1.6771
160	7.002e-04	2.1239	1.827e-02	1.9515	3.507e-02	1.8442
320	1.677e-04	2.0614	4.830e-03	1.9201	9.491e-03	1.8857

Fr = 0.1, $T = 1/6$

N	L^1-error in h	EOC	L^1-error in hu	EOC	L^1-error in hv	EOC
40	1.106e-04		2.614e-01		4.276e-01	
80	2.988e-05	1.8889	7.251e-02	1.8501	1.324e-01	1.6906
160	7.283e-06	2.0367	1.882e-02	1.9457	3.658e-02	1.8565
320	1.808e-06	2.0098	4.964e-03	1.9227	9.859e-03	1.8918

Fr = 0.01, $T = 1/6$

N	L^1-error in h	EOC	L^1-error in hu	EOC	L^1-error in hv	EOC
40	1.445e-06		2.617e-01		4.274e-01	
80	3.311e-07	2.1258	7.255e-02	1.8509	1.324e-01	1.6901
160	7.295e-08	2.1825	1.884e-02	1.9450	3.659e-02	1.8560
320	1.756e-08	2.0547	4.971e-03	1.9221	9.864e-03	1.8912

Fr = 0.001, $T = 1/6$

N	L^1-error in h	EOC	L^1-error in hu	EOC	L^1-error in hv	EOC
40	1.282e-08		2.564e-01		4.182e-01	
80	2.850e-09	2.1697	7.029e-02	1.8670	1.283e-01	1.7047
160	7.656e-10	1.8962	1.817e-02	1.9514	3.527e-02	1.8629
320	1.701e-10	2.1698	4.784e-03	1.9255	9.490e-03	1.8941

Table 1: Traveling vortex: L^1-errors and EOC for the ImEx 2 scheme for different Froude numbers Fr.

Grid	Fr = 1		Fr = 0.1		Fr = 0.01		Fr = 0.001	
	ImEx2	Explicit	ImEx2	Explicit	ImEx2	Explicit	ImEx2	Explicit
40 × 40	8.65	0.62	5.02	2.29	4.83	13.89	5.14	138.44
80 × 80	38.36	7.54	39.67	31.79	41.59	278.30	41.89	2,052.39
200 × 200	788.57	41.30	714.20	220.91	715.94	2,133.62	746.72	16,718.47

Table 2: Traveling vortex: CPU times in seconds consumed by the ImEx 2 and HLL-MUSCL-RK2 explicit schemes on different grids for different values of Fr. The final time is $T = 1/6$.

References

[1] U. M. Ascher, S. J. Ruuth, and B. T. R. Wetton. Implicit-explicit methods for time-dependent partial differential equations. *SIAM Journal on Numerical Analysis*, 32:797–823, 1995.

[2] E. Audusse, R. Klein, D. D. Nguyen, and S. Vater. Preservation of the discrete geostrophic equilibrium in shallow water flows. In J. Fořt, J. Fürst, J. Halama, R. Herbin, and F. Hubert, editors, *Finite Volumes for Complex Applications VI Problems & Perspectives*, pages 59–67, Berlin, Heidelberg, 2011. Springer Berlin Heidelberg.

[3] A. Bermudez, A. Dervieux, J. A. Desideri, and M. E. Vázquez. Upwind schemes for the two-dimensional shallow water equations with variable depth using unstructured meshes. *Computational Methods in Applied Mechanics and Engineering*, 155(1-2):49–72, 1998.

[4] A. Bermudez and M. E. Vazquez. Upwind methods for hyperbolic conservation laws with source terms. *Computers & Fluids*, 23(8):1049–1071, 1994.

[5] G. Bispen, K. R. Arun, M. Lukáčová-Medvid'ová, and S. Noelle. Imex large time step finite volume methods for low froude number shallow water flows. *Communications in Computational Physics*, 16(2):307–347, 2014.

[6] S. Boscarino and L. Pareschi. On the asymptotic properties of imex runge–kutta schemes for hyperbolic balance laws. *Journal of Computational and Applied Mathematics*, 316:60–73, 2017. Selected Papers from NUMDIFF-14.

[7] S. Boscarino, J.-M. Qiu, G. Russo, and T. Xiong. A high order semi-implicit imex weno scheme for the all-mach isentropic euler system. *Journal of Computational Physics*, 392:594–618, 2019.

[8] S. Boscarino and G. Russo. On a class of uniformly accurate imex runge-kutta schemes and applications to hyperbolic systems with relaxation. *SIAM J. Sci. Comput.*, 31(3):1926–1945, Mar. 2009.

[9] W. Boscheri. A space-time semi-lagrangian advection scheme on staggered voronoi meshes applied to free surface flows. *Computers & Fluids*, 202:104503, 2020.

[10] W. Boscheri, G. Dimarco, R. Loubère, M. Tavelli, and M.-H. Vignal. A second order all mach number imex finite volume solver for the three dimensional euler equations. *Journal of Computational Physics*, 415:109486, 2020.

[11] K. Brenner and C. Cancès. Improving newton's method performance by parametrization: The case of the richards equation. *SIAM Journal on Numerical Analysis*, 55(4):1760–1785, 2017.

[12] D. Bresch, R. Klein, and C. Lucas. Multiscale analyses for the shallow water equations. In E. Krause, Y. Shokin, M. Resch, D. Kröner, and N. Shokina, editors, *Computational Science and High Performance Computing IV*, pages 149–164, Berlin, Heidelberg, 2011. Springer Berlin Heidelberg.

[13] M. Brocchini and N. Dodd. Nonlinear shallow water equation modeling for coastal engineering. *Journal of Waterway, Port, Coastal, and Ocean Engineering*, 134(2):104–120, 2008.

[14] S. Busto and M. Dumbser. A staggered semi-implicit hybrid finite volume / finite element scheme for the shallow water equations at all froude numbers. *Applied Numerical Mathematics*, 175:108–132, 2022.

[15] V. Casulli. Semi-implicit finite difference methods for the two-dimensional shallow water equations. *Journal of Computational Physics*, 86(1):56–74, 1990.

[16] F. Couderc, A. Duran, and J.-P. Vila. An explicit asymptotic preserving low froude scheme for the multilayer shallow water model with density stratification. *Journal of Computational Physics*, 343:235–270, 2017.

[17] R. Danchin. Low mach number limit for viscous compressible flows. *ESAIM: M2AN*, 39(3):459–475, 2005.

[18] S. Dellacherie. Analysis of godunov type schemes applied to the compressible euler system at low mach number. *Journal of Computational Physics*, 229(4):978–1016, 2010.

[19] S. Dellacherie, J. Jung, P. Omnes, and P.-A. Raviart. Construction of modified godunov-type schemes accurate at any mach number for the compressible euler system. *Mathematical Models and Methods in Applied Sciences*, 26(13):2525–2615, 2016.

[20] G. Dimarco, R. Loubère, and M. H. Vignal. Study of a new asymptotic preserving scheme for the euler system in the low mach number limit. *SIAM J. Sci. Comput.*, 39, 2017.

[21] G. Dimarco, R. Loubère, V. Michel-Dansac, and M.-H. Vignal. Second-order implicit-explicit total variation diminishing schemes for the euler system in the low mach regime. *Journal of Computational Physics*, 372:178–201, 2018.

[22] F. Dubois and P. G. LeFloch. Boundary conditions for nonlinear hyperbolic systems of conservation laws. *Journal of Differential Equations*, 71:93–122, 1988.

[23] M. Dumbser and V. Casulli. A staggered semi-implicit spectral discontinuous galerkin scheme for the shallow water equations. *Applied Mathematics and Computation*, 219(15):8057–8077, 2013.

[24] A. Duran, F. Marche, R. Turpault, and C. Berthon. Asymptotic preserving scheme for the shallow water equations with source terms on unstructured meshes. *Journal of Computational Physics*, 287:184–206, 2015.

[25] P. García-Navarro, J. Murillo, J. Fernández-Pato, et al. The shallow water equations and their application to realistic cases. *Environmental Fluid Mechanics*, 19(5):1235–1252, 2019.

[26] J.-F. Gerbeau and B. Perthame. Derivation of viscous saint-venant system for laminar shallow water; numerical validation. *Discrete and Continuous Dynamical Systems - B*, 1(1):89–102, 2001.

[27] E. Godlewski, M. Parisot, J. Sainte-Marie, and F. Wahl. Congested shallow water model: roof modeling in free surface flow. *ESAIM: M2AN*, 52(5):1679–1707, 2018.

[28] E. Godlewski, M. Parisot, J. Sainte-Marie, and F. Wahl. Congested shallow water model: on floating body. *The SMAI Journal of computational mathematics*, 6:227–251, 2020.

[29] E. Godlewski and P.-A. Raviart. *Hyperbolic systems of conservation laws*. Number 3-4. Ellipses, 1991.

[30] S. Gottlieb, C.-W. Shu, and E. Tadmor. Strong stability-preserving high-order time discretization methods. *SIAM Review*, 43(1):89–112, 2001.

[31] N. Goutal. *Proceedings of the 2nd workshop on dam-break wave simulation*. Department Laboratoire National d'Hydraulique, Groupe Hydraulique Fluviale, 1997.

[32] N. Grenier, J.-P. Vila, and P. Villedieu. An accurate low-mach scheme for a compressible two-fluid model applied to free-surface flows. *Journal of Computational Physics*, 252:1–19, 2013.

[33] H. Guillard and A. Murrone. On the behavior of upwind schemes in the low mach number limit: Ii. godunov type schemes. *Computers & Fluids*, 33(4):655–675, 2004.

[34] H. Guillard and C. Viozat. On the behaviour of upwind schemes in the low mach number limit. *Computers & Fluids*, 28(1):63–86, 1999.

[35] J. Haack, S. Jin, and J. Liu. An all-speed asymptotic-preserving method for the isentropic euler and navier-stokes equations. *Communications in Computational Physics*, 12(4):955–980, 2012.

[36] S. Jin. Runge-kutta methods for hyperbolic conservation laws with stiff relaxation terms. *Journal of Computational Physics*, 122(1):51–67, 1995.

[37] S. Jin and L. Pareschi. Asymptotic-preserving (ap) schemes for multiscale kinetic equations: a unified approach. In H. Freistühler and G. Warnecke, editors, *Hyperbolic Problems: Theory, Numerics, Applications*, pages 573–582, Basel, 2001. Birkhäuser Basel.

[38] S. Klainerman and A. Majda. Singular limits of quasilinear hyperbolic systems with large parameters and the incompressible limit of compressible fluids. *Communications on Pure and Applied Mathematics*, 34:481–524, 1981.

[39] S. Klainerman and A. Majda. Compressible and incompressible fluids. *Communications on Pure and Applied Mathematics*, 35:629–651, 1982.

[40] P. D. Lax and B. Wendroff. Systems of conservation laws. *Communications on Pure and Applied Mathematics*, 13:217–237, 1960.

[41] O. Le Maître, J. Levin, M. Iskandarani, and O. M. Knio. A multiscale pressure splitting of the shallow-water equations: I. formulation and 1d tests. *Journal of Computational Physics*, 166(1):116–151, 2001.

[42] R. J. LeVeque. Balancing source terms and flux gradients in high-resolution godunov methods: The quasi-steady wave-propagation algorithm. *Journal of Computational Physics*, 146(1):346–365, 1998.

[43] Q. Liang and A. G. Borthwick. Adaptive quadtree simulation of shallow flows with wet-dry fronts over complex topography. *Computers & Fluids*, 38(2):221–234, 2009.

[44] M.-S. Liou. A sequel to ausm, part ii: Ausm+-up for all speeds. *Journal of Computational Physics*, 214(1):137–170, 2006.

[45] X. Liu, A. Chertock, and A. Kurganov. An asymptotic preserving scheme for the two-dimensional shallow water equations with coriolis forces. *Journal of Computational Physics*, 391:259–279, 2019.

[46] R. Lteif. Well-balanced numerical resolution of the two-layer shallow water equations under rigid-lid with wet–dry fronts. *Computers & Fluids*, 235:105277, 2022.

[47] J. Murillo, P. Garcia-Navarro, and J. Burguete. Time step restrictions for well-balanced shallow water solutions in non-zero velocity steady states. *International Journal for Numerical Methods in Fluids*, 60:1351–1377, 2009.

[48] L. Pareschi and G. Russo. Implicit–explicit runge–kutta schemes and applications to hyperbolic systems with relaxation. *Journal of Scientific Computing*, 25:129–155, 2005.

[49] M. Parisot. Congested shallow water model: Trapped air pockets modeling. *SIAM Journal on Scientific Computing*, 45(6):B828–B852, 2023.

[50] M. Parisot and J.-P. Vila. Centered-potential regularization for the advection upstream splitting method. *SIAM Journal on Numerical Analysis*, 54(5):3083–3104, 2016.

[51] C. Parés and C. Parés-Pulido. Well-balanced high-order finite difference methods for systems of balance laws. *Journal of Computational Physics*, 425:109880, 2021.

[52] M. Ricchiuto, R. Abgrall, and H. Deconinck. Application of conservative residual distribution schemes to the solution of the shallow water equations on unstructured meshes. *Journal of Computational Physics*, 222(1):287–331, 2007.

[53] M. Ricchiuto and A. Bollermann. Stabilized residual distribution for shallow water simulations. *Journal of Computational Physics*, 228(4):1071–1115, 2009.

[54] X. song Li and C. wei Gu. An all-speed roe-type scheme and its asymptotic analysis of low mach number behaviour. *Journal of Computational Physics*, 227(10):5144–5159, 2008.

[55] E. F. Toro, C. E. Castro, D. Vanzo, and A. Siviglia. A flux-vector splitting scheme for the shallow water equations extended to high-order on unstructured meshes. *International Journal for Numerical Methods in Fluids*, 94(10):1679–1705, 2022.

[56] B. van Leer. Towards the ultimate conservative difference scheme. v. a second-order sequel to godunov's method. *Journal of Computational Physics*, 32(1):101–136, 1979.

[57] S. Vater and R. Klein. A semi-implicit multiscale scheme for shallow water flows at low froude number. *Communications in Applied Mathematics and Computational Science*, 13(2):303–336, 2018.

[58] H. Zakerzadeh. Asymptotic analysis of the rs-imex scheme for the shallow water equations in one space dimension. *ESAIM: M2AN*, 53(3):893–924, 2019.